## EUROPEAN ORGANIZATION FOR NUCLEAR RESEARCH

# **Time Projection Chambers**

### H. J. HILKE

#### **Abstract**

The Time Projection Chamber (TPC) had originally been proposed to permit full reconstruction of events of up to 20 particles at an electron-positron collider. It was to provide 3-D information for tracking and momentum measurement together with particle identification by multiple ionization sampling, in a compact detector. This powerful combination soon found applications in other fields: at one end, for studies of rare events of simple structure; at the other extreme, for heavy ion collisions, handling ever higher particle densities, finally up to several thousand tracks in a single event, still providing information on a track-to-track basis.

Basic physics, performance and limitations of drift chambers in general will be discussed first. Then the characteristics of TPCs will be introduced, as well as their practical realization and performance. The development from the first TPC, 30 years ago, to the present day will be covered and followed by a few final comments on the ongoing studies for future applications.

Invited review, accepted for publication by IOP Publishing: Rep. Prog. Phys. 73 (2010) 116201

#### **Contents**

- 1. Introduction
- 2. General Properties of Drift Chambers
  - 2.1. Gas ionization by charged particles
    - 2.1.1. Primary Clusters
    - 2.1.2. Total ionization-dE/dx
    - 2.1.3. Effective number of electrons  $N_{eff}$
  - 2.2. Transport of electrons and ions
    - 2.2.1. Drift velocities
      - Drift of electrons
      - Drift of ions
      - Magnetic field effects
    - 2.2.2. Diffusion
      - Isotropic diffusion
      - Anisotropic diffusion
    - 2.2.3. Electron attachment
  - 2.3. Signal formation
    - 2.3.1. Signal induction
    - 2.3.2. Gas amplification
  - 2.4. Calibration with laser beams
  - 2.5. Ageing of wire chambers
- 3. TPC characteristics
  - 3.1. Basic design PEP4 TPC
  - 3.2. Specific aspects
    - 3.2.1. Wire chamber layout
    - 3.2.2. Sector boundaries
    - 3.2.3. Gating
    - 3.2.4. Field cages
    - 3.2.5. Calibration
    - 3.2.6. Choice of gas mixture
    - 3.2.7. Electronics
  - 3.3. Performance
    - 3.3.1. Spatial resolution
    - 3.3.2. Particle identification-dE/dx
  - 4. Particularities of some TPCs
    - 4.1. Global aspects
    - 4.2. Special aspects
    - 4.3. Radial/spherical geometries
  - 5. Gas amplification without anode wires
    - 5.1. Parallel plate chamber
    - 5.2. Micromegas
    - 5.3. GEM
  - 6. Conclusions

#### 1. Introduction

The Time Projection Chamber is the only electronically read gaseous detector delivering direct three-dimensional track information: for each point on the track, x-,y- and z-coordinates are measured simultaneously. This is of particular importance for pattern recognition in high multiplicity events. The combination of powerful tracking with particle identification capacity over a wide momentum range, based on multiple measurements of ionization loss, is the trademark of the TPC. The timely appearance on the market of an affordable multi-sample analog memory, the CCD, was an essential ingredient. The major limitation is high event rate.

In 1968, when bubble chambers and spark chambers dominated the field of tracking detectors in High Energy Physics, multiwire proportional chambers (MWPC) [1] and almost simultaneously drift chambers (DC) [2, 3] were introduced, with the principal aim of increasing data taking rates. The rapid progress in semiconductor electronics, which had started only a decade before with slow devices, made possible the fast readout of hundreds and soon thousands of signal channels at affordable cost. This was an essential ingredient to an extremely rapid development of both detector technologies: many different layouts were used and size and complexity of the designs grew constantly. In 1972 already, a MWPC system containing 50 000 wires was under construction. Only 3 years later, the Time Projection Chamber (TPC) was proposed by David Nygren [4], a drift chamber providing simultaneously non-projective track recognition, momentum measurement and particle identification in a compact device.

The basic idea for a detector to be installed around the interaction point of an electron-positron collider was to take a long gas-filled cylinder, with a thin HV electrode in the centre, negatively charged with respect to the Multiwire Proportional Chambers (MWPC)s used for readout at both ends. The electrons produced along the path of a charged particle traversing the cylinder are drifting to the MWPC and pass through a grid into the multiplication region. They form avalanches near the anode wires. The cathode underneath the wires is segmented into pads and the pulses induced by the avalanches are registered in addition to those from the anode wires. The anode wires are arranged azimuthally around the cylinder axis and their signals provide the radial coordinate. The pads provide the hit coordinate along the wires above them. The third coordinate is obtained from the arrival time of the signals.

Care is taken to produce a homogeneous electric field E along the axis of the cylinder and to align this parallel to the magnetic field B of the solenoid surrounding the TPC, in order to provide an undeformed projection of the original ionization track onto the MPWC plane. A strong magnetic field is necessary for the momentum measurement but is in many cases also useful to improve the point measuring precision due to reduced transverse diffusion. Particle identification is obtained by taking many samples of the track ionization (dE/dx), from the pulse height measurements on the wires or pads.

The first TPC, as part of the PEP4 experiment at SLAC, started taking data in 1983. Rather rapidly, other TPCs were constructed and many followed since, in collider and fixed-target experiments with increasing particle multiplicities. The dimensions grew for some of them significantly, the number of read-out channels even more, encouraged by the fast developments in electronics. This enabled track reconstruction of events with extremely high particle multiplicities, taking full advantage of the unique pattern recognition capabilities. In parallel, the TPC technique found applications in searches for rare and exotic processes with low multiplicities.

We shall start with a discussion of properties applying to drift chambers in general and then describe particular properties and the performance of TPCs.

The TPC developments until 1992 can be found in a detailed review [5], recent short overviews in [6],

The following terms and numbers will appear repeatedly:

STP = standard temperature and pressure :  $0^{\circ}$  C and 1 atm (this is the most commonly used definition of STP, although the new convention of IUPAC demands 1bar = 1atm / 1.01325).

Avogadro constant  $N_A = 6.022 * 10^{23}$  molecules per mole.

 $N \cong 2.68 * 10^{19}$  mol. / cm<sup>3</sup> = Number of molecules per cm<sup>3</sup> for an ideal gas at STP; densities of most detector gases at STP are very close to the ideal gas density (e.g. Ar, Ne, CH<sub>4</sub>, CO<sub>2</sub>).

Thermal energy =  $3kT / 2 \cong 0.0353$  eV at STP.

1 Townsend = 1Td =  $10^{-17}$  Vcm<sup>2</sup>  $\cong 269$  V / (cm atm) at 0°C and 251 V / (cm atm) at 20°C (NTP). Relative speed of a particle  $\beta = v / c_0$ , where  $c_0$  is the speed of light in vacuum;  $\gamma = (1-\beta^2)^{-1/2}$ . A mip = minimum ionizing particle with  $\gamma \sim 3.5$  (the minimum of ionization is rather broad).

Cyclotron frequency  $\omega = eB / m \approx 1.76*10^{11} / s$  for electrons in a magnetic field B = 1T.

### 2. General Properties of Drift Chambers

A detailed discussion of all aspects of drift chambers is presented in [7]. We shall repeatedly refer to this book. A recent account of signal processing also applying to gaseous detectors may be found in [8]. An early overview of wire chamber properties is given in [26].

Powerful simulation programs have been developed and agreement with experimental results has become impressive. The program *Heed* [9] calculates primary ionization produced by fast particles in gases; *Garfield* [10] electric fields, electron and ion trajectories and induced signals and *Magboltz* [11] electron transport properties like drift velocities and diffusion. These programs are of great help in the planning and optimization of detector setups and operation parameters and for the interpretation of the results.

### 2.1 Gas ionization by charged particles

### 2.1.1 Primary clusters

A charged particle crossing the detector loses energy by excitation and ionization of the detector gas, in similar amounts. The ionizing collisions occur randomly, their number k in a *segment s* along the track following Poisson statistics

$$P(k) = ((s / \lambda)^k / k!) \exp(-s / \lambda)$$
, (2.1)

where  $\lambda=1$  /  $(N_e\sigma_i)$  is the mean distance between clusters,  $N_e$  the electron density of the gas and  $\sigma_I$  the ionization cross-section per electron. The probability to find no cluster in s is  $P(0)=\exp{(-s/\lambda)}$ , the probability to find no cluster in s but one in  $\delta s$  is  $(\delta s/\lambda)\exp{(-s/\lambda)}$ , i.e. short distances are favoured.

Most ionizing collisions (about 66% in Argon) produce only a single electron/ion pair. In the other collisions, however, the primary electron receives enough kinetic energy to liberate one or more secondary electrons on other molecules. As the kinetic energies involved are small in most cases, the secondary electrons usually stay close to the first electron/ion pair, forming a 'cluster'. In rare collisions, electrons are ejected with high energy, so-called ' $\delta$ -electrons', which leave a detectable ionization trail off the particle trajectory. The average number per cm of energetic electrons with energy E>E<sub>0</sub> is approximately inversely proportional to E<sub>0</sub>:

$$P(E>E_0) \sim y / (\beta^2 E_0) / cm,$$
 (2.2)

with E in keV and y = 0.114 for Ar and y = 0.064 for Ne [12],  $\beta$  = v / c. This gives P=0.011/cm for  $\beta$  = 1 and E<sub>0</sub> =10 keV in Ar., i.e. one collision with E>10 keV in 90 cm on average. The practical range R<sub>p</sub> of a 10 keV electron is about 1.4 mm. As R<sub>p</sub> is roughly proportional to E<sup>1.65</sup> in the energy range 1-40 keV, the range for a 1 keV electron is only about 30  $\mu$ m .

Although most of the 'clusters' contain only one electron, clusters with more electrons contribute significantly to the mean total number  $n_T$  of electrons per cm: one finds  $n_T >> n_p = 1 / \lambda$ , the mean number of clusters per cm. For many years there existed only one detailed study providing theoretical estimates for the cluster size distribution [13]. Finally, experimental values have been obtained for cluster sizes up to 18 electrons in Ar, CH<sub>4</sub> and a few other gases, see figure 1 [14]. Table 1 presents some of the experimental and theoretical results.

**Table 1.** Measured [14] and theoretical [13] cluster size distributions

Cluster size	1	2	3	4	5	6	7	8	9	10
Meas. Ar	66	15	6.4	3.5	2.3	1.6	1.1	0.8	0.6	0.5
Meas. CH4	79	12	3.4	1.6	1	0.6	0.4	0.3	0.3	0.2
Theor. Ar	80	7.7	2	1.3	0.8	0.6	0.5	0.6	0.8	0.9

In Ar one finds on average some 25 clusters / cm with a total  $n_T$  of about 100 electrons/cm. The most probable value for the total number of electrons is  $n_{mp}$ = 42 electrons / cm. The large difference between the mean and the most probable value is caused by the long tail of the cluster distribution. In fact, the largest kinetic energy which can be transmitted to an electron by a heavy particle of mass M and momentum  $\gamma\beta$ cM is:

$$T_{\text{max}} = 2 \text{ m}_{\text{e}} c^2 \beta^2 \gamma^2 / B ;$$
 (2.3)

With  $B = 1 + (2 \gamma m_e / M) + (m_e / M)^2 \rightarrow 1$  for  $2\gamma m_e / M << 1$ .

It follows that a 1GeV proton can transmit a maximum of about 1 MeV to an electron, but with a probability of only about  $10^{-5}$  / cm in Ar.

Both the Poisson distribution of the clusters along the particle track and the cluster size distribution influence the spatial resolution in a drift chamber, whether it is determined by the arrival time of the first n electrons or by centre-of-gravity calculation from induced pulses. In addition, energetic  $\delta$ -electrons can produce signals significantly off the track.

### 2.1.2 Total ionization - dE/dx

Over a wide energy range, elementary particles heavier than electrons lose energy predominantly by atomic excitation and ionization, whilst for electrons bremsstrahlung becomes dominant already at relatively low energies. The mean energy loss for heavy particles of charge z in detectors is well described by the *modified Bethe-Bloch equation* [15, p. 268]:

$$< dE / dx > = Kz^{2} (Z / A)(1/\beta^{2})[0.5 ln(2m_{e}c^{2}\beta^{2}\gamma^{2}T_{max}/I^{2}) - \beta^{2} - \delta/2],$$
 (2.4)

where  $K = 4\pi N_A r_e 2 m_e c_0^2$ ,  $N_A = Avogadro$  constant,  $m_e$ ,  $r_e$  are the mass and classical radius of the electron and I is the mean excitation energy of the atom.

The energy loss is a function only of the particle velocity  $\beta$ , except for a minor dependence on the particle mass through the maximum energy transfer  $T_{max}$ . A minimum ionizing particle (mip) has  $\beta \gamma = 3-4$  and a minimum energy loss per cm of 1-2 MeVg<sup>-1</sup>cm<sup>2</sup> for all materials, except for hydrogen with 4 MeVg<sup>-1</sup>cm<sup>2</sup> loss. The minimum is followed at higher energies by a logarithmic rise which tends to level off faster for denser materials as described by the density correction  $\delta$  (being a function of  $\beta \gamma$ ).

The translation into ionization is obtained by introducing w, the mean energy lost to produce an electron/ion pair:  $w = \frac{dE}{dx} / n_T$ .

It turns out that w is rather independent of particle energy, except for the lowest energies (<100 eV for electrons, <10-30 keV for protons and below some MeV for  $\alpha$ -particles) [16]. In rare gases (except possibly for He) the values are also very close for different particles, from electrons to  $\alpha$ -particles; for some organic vapours they are up to 15% higher for  $\alpha$ -particles. For rare gases one finds w = (1.4-1.8)  $E_I$  and for common molecular gases w = (2.1-2.5)  $E_I$ , see Table 2. The difference to the ionization energy  $E_I$  is the result of losses due to excitation and to slow electrons with kinetic energies below the first excitation level.

In a gas mixture with one component A having an excitation level higher than the ionization level of component B, excited molecules of A often induce significant additional ionization of B molecules, as observed e.g. in He and Ne even with minute impurities: the addition of 0.13% Ar to He changed w from 41.3 to 29.7 eV per ion pair. This energy transfer is called *Jesse effect*, or *Penning effect*, when metastable states are involved.

The Bethe-Bloch equation describes the totality of losses, including those of  $\delta$ -electrons with energies up to the maximum possible energy  $T_{max}$ . These electrons may leave the sensitive zone of a detector element. As one is interested in the ionization near to the particle trajectory, it is sensible to replace  $T_{max}$  by a cut-off energy  $T_{cut}$ . This leads to the formula for the *mean restricted energy loss* for  $T_{cut} << T_{max}$  [15, p.270].

$$< dE / dx_{restricted} > = K z^{2} (Z / A)(1/\beta^{2}) [0.5 ln (2m_{e}c^{2}\beta^{2}\gamma^{2}T_{cut}/I^{2}) - \beta^{2}/2 - \delta/2],$$
 (2.5)

The cut-off obviously depends on the readout technique and could lie around 10-50 keV outside a magnetic field and higher inside. Assuming w is independent of the particle energy for a given gas, the *ionization measured* in the detector should follow the restricted energy loss. That means, that for a sample of length L along the particle trajectory, the mean total number of electrons deposited is:

$$\langle n(L) \rangle = L \langle dE / dx_{restricted} \rangle / w = n_T L$$
. (2.6)

Figure 2 shows a measured relativistic rise and the plateau [17] in  $Ar/CH_4$  (90/10) compared to simulation [18] and figure 3 the density effect for various gas pressures [19]. The lowering of the Fermi-plateau for higher pressure is significant.

The distribution of n(L) for small samples L is very broad, with a long tail towards the high energies, caused by energetic  $\delta$ -rays, see figure 4. The mean and variance of this distribution are, therefore, ill-defined and it is better to characterize the pulse height distribution of the sample by its *most probable number of electrons/cm*,  $n_{mp}$ , and its full-width-half-mean, *FWHM*. To obtain a reasonable accuracy on  $n_{mp}$  for particle identification by dE/dx, many samples are required, see chapter 3.3.2.

Table 2 shows experimental values for some of the common detector gases for a minimum ionizing particle (mip). Results from different measurements vary up to a few percent for  $n_T$ , w and in particular for  $n_D$ , as cluster separation is experimentally difficult.

**Table 2.** Properties of gases at 20°C, 1atm.  $n_p$ ,  $n_T$ : mean primary and total number of electronion pairs per cm; w: average energy dissipated per ion pair; E<sub>I</sub>, E<sub>x</sub>: lowest ionization and

excitation	energies	115	n 2921
CACITATION	CHCLETCS	110,	P. 2/2  .

Gas	$n_p$	$n_T$	w (eV)	$E_{I}(eV)$	$E_{x}(eV)$	$\rho$ (mg/cm <sup>3</sup> )
He	4.8	7.8	45	24.5	19.8	0.166
Ne	13	50	30	21.6	16.7	0.84
Ar	25	100	26	15.7	11.6	1.66
Xe	41	312	22	12.1	8.4	5.50
$CH_4$	37	54	30	12.6	8.8	0.67
$C_2H_6$	48	112	26	11.5	8.2	1.26
i-butane	90	220	26	10.6	6.5	2.49
$CO_2$	35	100	34	13.8	7.0	1.84
CF <sub>4</sub>	63	120	54	16.0	10.0	3.78

### **2.1.3.** Effective number of electrons $N_{eff}$ .

Due to the electron clustering, for several quantities of interest to us, the number of electrons relevant is the number  $N_{\text{eff}}$  of independently acting electrons and not the total number. We follow some of the arguments of [7].

Take the simple case of a track segment L and determine the precision of the centre of gravity of the charge deposition, assuming m pointlike clusters with n<sub>i</sub> electrons are deposited at x<sub>i</sub>. The centre of gravity is

$$X_{cg} = \sum (x_i n_i) / \sum n_i = \sum (x_i n_i) / N$$
 (2.7)

The sum goes from 1 to m, N is the total number of electrons in L. Let x = 0 be the centre of L. The probability distribution for each x; is

$$F(x_i) dx_i = (1/L) dx_i$$
 (2.8)

For every fixed 
$$n_i$$
 the average is  $\langle x_{cg} \rangle = 0$  and  $\langle x_{cg}^2 \rangle = \langle \sum x_i^2 n_i^2 \rangle / N^2$   
=  $(L^2 / 12) (\sum n_i^2) / N^2 = (L^2 / 12) / N_{eff}$ , (2.9)

as definition of N<sub>eff</sub> with

$$N_{\text{eff}} = N^2 / (\sum n_i^2)$$
. (2.10)

 $N_{eff}$  is always  $\leq$  m. Take as an extreme case m = 2 clusters with  $n_2 \gg n_1$ . Then  $N_{eff}$  is close to 1, as the effect of the small cluster is negligible. For the cluster distribution calculated by [13], approximately  $N_{\text{eff}} = m^{0.54}$  has been obtained [7].

The values of N<sub>eff</sub> are thus very small for situations with well separated clusters. This changes when clusters start mixing through diffusion. In the limit of very large diffusion, Neff will approach the total number N of electrons. This declustering through diffusion has been observed [20] and simulated [7]. For a mean distance between clusters of 1/m = 0.37 mm, the cluster distribution of [13] and a sample length of 4mm, the simulation indicates  $N_{\text{eff}} = 0.3$  times m without diffusion, equal to m for rms diffusion of 1.6 mm and twice m for diffusion of 4 mm.

A similar effect is caused by the fluctuations in the gas amplification and in practice these two effects are combined. The combined action on the spatial resolution from centroid determination in the TPC has been analyzed in detail and compared to measurements [21].

### 2.2 Transport of Electrons and Ions

In this chapter, only the main results can be presented, often without derivation. A detailed account of drift chamber properties is given in [7], to which we shall refer at several occasions. Without external fields, electrons and ions will be in thermal equilibrium and their movement will be described by a mean *instantaneous velocity* v given by  $(m/2)v^2 = (3/2)$  kT and an isotropic diffusion coefficient D. When an electric field E is applied, electrons and ions will acquire drift velocities u antiparallel, resp. parallel to E, with u much smaller than v. In the presence of an additional magnetic field, the drift directions will be determined by both E and E. Diffusion will no more be isotropic but will show a coefficient for longitudinal diffusion  $D_L$ , along E, which may be quite different from  $D_T$ , describing diffusion at right angles to E. The big mass difference between electrons and ions results in very different behaviour.

In the following chapters, a simple model will bring out the main characteristics and explain qualitatively the results from measurements. This model is based on the approximation of a single instantaneous velocity v and a single effective cross-section  $\sigma(v)$  describing the elastic and inelastic spectrum. More rigorous treatments including the distribution of v around its mean value achieve quantitative agreement with measurement for many cases.

#### 2.2.1. Drift velocities

#### 2.2.1.1. Drift of electrons

When moving in a gas, electrons –because of their light mass- scatter isotropically and forget any preferential direction after each collision with an atom. If an electric field E is present in the drift volume, an electron will be accelerated between collisions and acquire a *drift velocity* u, which is equal to the acceleration times the average time  $\tau$  since the last collision,  $\tau$  being also the mean time between collisions:

$$u = eE\tau / m \tag{2.10}$$

The mobility  $\mu$ , defined by  $u=\mu E$ , is not constant, as  $\tau$  depends on E.

In the next collision, the electron will lose a fraction  $\Delta$  of the energy  $\epsilon_E$  picked up between collisions and over a distance x there will be a balance between the energy lost and the energy gained:

$$(x/u)(1/\tau)\Delta \varepsilon_E = e E x, \qquad (2.11)$$

as  $(x/u)(1/\tau)$  is the number of collisions over a distance x.

The mean time  $\tau$  between collisions is related to the collision cross-section  $\sigma$  per molecule, the number density N of gas molecules and the *mean instantaneous velocity* v by

$$(1/\tau) = N \sigma v \tag{2.12}$$

Including the thermal energy, the total energy  $\varepsilon$  of the electron is given by

$$\varepsilon = \varepsilon_E + (3/2) kT = (m/2) v^2$$
 (2.13)

In particle detectors, the approximation  $\varepsilon >> (3/2)kT$  for drifting electrons is fulfilled for many gases; these gases – like Ar and CH<sub>4</sub> – are called 'hot' gases in contrast to 'cold' gases as  $CO_2$  with  $\varepsilon$  close to (3/2)kT. One then obtains

$$u^{2} = (eE / mN\sigma) \sqrt{(\Delta / 2)}$$
 and (2.14)

$$v^2 = (eE / mN\sigma)\sqrt{(2/\Delta)}$$
 for  $\varepsilon \sim \varepsilon_E \gg (3/2) kT$  (2.15)

A more rigorous theory assuming a Dryvestern distribution for the random velocities v adds a multiplication factor of about 0.85 to the right sides [7]. To achieve accuracies of a percent or better, it is necessary to go one step further and to apply a multiterm ( $n \ge 4$ ) spherical harmonic expansion treatment of the Boltzmann equation [22] or use Monte Carlo, as done in the present Magboltz 2 [11].

As can be seen, E and N only appear as E/N, the reduced electric field. A special unit, the Townsend (Td), is often used for E / N:  $1 Td=10^{-17} V cm^2$ .

Both  $\sigma$  and  $\Delta$  depend on  $\varepsilon$ . For energies  $\varepsilon$  below the first excitation level, the scattering is elastic and  $\Delta \sim 2\text{m/M} \sim 10^{-4}$  for molecules of mass M. Low  $\sigma$  and large  $\Delta$  are required for high drift speeds. An example of a low  $\sigma$  is the so-called 'Ramsauer dip' in the cross-section  $\sigma$ observed in heavy rare gases and in CH<sub>4</sub>, see figure 5 [23], which leads to high drift velocities in Ar-CH<sub>4</sub> mixtures at low E-values. This was an important reason for the choice of these gases in several TPCs.

For gas mixtures with number densities  $n_i$  (N =  $\sum n_i$ ), the effective  $\sigma$  and  $\Delta$  are given by

$$\sigma = \sum n_i \sigma_i / N \quad \text{and}$$

$$\Delta \sigma = \sum n_i \Delta_i \sigma_i / N$$
(2.16)
(2.17)

$$\Delta \sigma = \sum n_i \, \Delta_i \sigma_i / N \tag{2.17}$$

For some gases,  $\sigma$  and  $\Delta$  have been calculated from precise measurements of drift velocity u (to 1%) and diffusion D/ $\mu$  (to 3-5%), see e.g. [24]. Figure 6 shows the *characteristic energy*  $\varepsilon_k$ (2/3) ε derived in another study [25] in the same way for two extreme cases, 'cold' CO<sub>2</sub> and a 'hot' Ar. In 'cold' gases electrons lose energy to low vibrational and rotational levels, which keeps  $\varepsilon$  low. Figure 7 presents calculated values for  $\Delta$  as function of  $\varepsilon$  [24].

Drift velocities for different gas mixtures show very different values and dependence on the electric field. At low fields, they in general rise with electric field. Then for many gases they go through a more or less pronounced maximum and minimum before rising again. Drift velocities are shown in Figure 8 for a few gases [15, 26]. For a large number of gas mixtures, velocities calculated with Magboltz 2 vs. 7.1 can be found in [33].

#### 2.2.1.2 **Drift of ions**

A detailed account of mobility and diffusion of ions in gases is given in [27]. Because of their heavy mass  $m_i$ , ions lose a significant fraction  $\Delta$  of their energy in a collision with a gas molecule M (on average  $\Delta = 2m_iM/(m_i + M)^2$ ), so that their random energy will stay close to thermal energy and the momentum will only be partially randomized. As a result, diffusion will be much smaller than for electrons and the mobility will stay constant up to high fields E.

For particle detectors, the low E-field approximation is valid, except in the regions of high gas amplification. The random velocity is taken as thermal, i.e. the relative velocity v<sub>rel</sub> between the ion and the gas molecules of masses m; and M, respectively, is assumed to be

$$v_{rel}^2 = v_{ion}^2 + v_{gas}^2 = 3 \text{ kT} (m_i^{-1} + M^{-1})$$
 (2.18)

The average time between collisions is  $\tau = 1 / (N\sigma v_{rel})$  and an argumentation similar to the one followed for electrons [7] leads to

$$u = (m_i^{-1} + M^{-1})^{1/2} (3 kT)^{-1/2} e E / (N\sigma) .$$
 (2.19)

At low E-fields, the drift velocities are proportional the E/N and the mobilities are constant, as  $\sigma$ is practically constant in the energy spectrum of the ions. A typical value is  $u \sim 2$  m/s for CH<sub>4</sub> at E = 100 V/cm atm, to be compared with a thermal velocity around 650 m/s at STP.

For very high E-fields, the drift velocities are proportional to the square root of E / N or of E/p, if temperature is kept constant. Figure 9 shows measured values for E/p in noble gases: both extremes are visible, with a transition for Ar between 25 and 150 kV / cm atm.

In gas mixtures it is expected that after a short distance of the order of a cm only the species with the lowest ionization energy is left over from the various ion types produced originally, because the charge transfer cross-sections are big and similar to other ion-molecule scattering cross-sections [120]. Measurements in binary and ternary mixtures support this assumption, showing a simple relation (Blanc's law) for the ion mobility  $\mu$ :

$$1 / \mu = \sum p_k / \mu_k$$
 (2.20)

where  $p_k$  are the volume concentrations of the components and  $\mu_k$  the mobilities in the component k [25]. This relation is expected, if the type of drifting ions does not change.

In an argon-isobutane-methylal mixture the charge exchange from isobutane to methylal becomes inefficient only for concentrations of methylal below about 3%.

#### 2.2.1.3 Magnetic field effects

Langevin has derived a relation providing a good approximation for many practical cases:

$$\mathbf{u} = (e/m) \tau | \mathbf{E} | (1 / (1 + \omega^2 \tau^2)) \{ \mathbf{E}^* + \omega \tau [\mathbf{E}^* \times \mathbf{B}^*] + \omega^2 \tau^2 (\mathbf{E}^* \bullet \mathbf{B}^*) \mathbf{B}^* \},$$
 (2.21)

where m, e and **u** are the particle's mass, charge and velocity vector; **E** and **B** the electric and magnetic field vectors ( $\mathbf{E}^*$  and  $\mathbf{B}^*$  are unit vectors);  $\boldsymbol{\omega} = (e/m) \mid \mathbf{B} \mid$  and carries the sign of e;  $\boldsymbol{\tau}$  is the *mean time between collisions*.

For ions,  $\omega \tau \sim 10^{-4}$ . Therefore, magnetic fields have negligible effect on ion drift.

For electrons, **u** is along **E**, if B=0, with

$$\mathbf{u} = (\mathbf{e} / \mathbf{m}) \, \mathbf{\tau} \, \mathbf{E} , \qquad (2.22)$$

the same relation which was derived in 2.2.1.1.

For large  $\omega \tau$ , i.e. large B, **u** tends to be along **B**, but if  $\mathbf{E} \bullet \mathbf{B} = 0$ , large  $\omega \tau$  turns u in the direction of  $\mathbf{E} \times \mathbf{B}$ .

In drift chambers, two cases are of particular interest:

### E orthogonal to B

With  $\mathbf{E} \bullet \mathbf{B} = 0$  and choosing  $\mathbf{E} = (\mathbf{E}_x, 0, 0)$  and  $\mathbf{B} = (0, 0, \mathbf{B}_z)$ , we get

$$u_x = (e/m) \tau |E| / (1+\omega^2 \tau^2) ,$$
 (2.23)

$$u_v = -(e/m) \tau \omega \tau |E| / (1 + \omega^2 \tau^2)$$
, (2.24)

$$u_z = 0 \quad \text{and} \tag{2.25}$$

$$tg\psi = u_v / u_x = -\omega \tau . \qquad (2.26)$$

From a measurement of this *Lorentz angle*  $\psi$ ,  $\tau$  can be obtained. As  $\psi$  leads to an increased spread of arrival times and sometimes also increases the lateral spread, a small  $\omega\tau$  would help, but momentum resolution usually requires a strong B.

The absolute value of  $\mathbf{u}$  is

$$|\mathbf{u}| = (e/m) \tau |\mathbf{E}| (1 + \omega^2 \tau^2)^{-1/2} = (e/m) \tau |\mathbf{E}| \cos \psi . \tag{2.27}$$

The component of E along u determines the drift velocity (Tonks' theorem), independent of the drift direction. This is well verified by experiments.

#### E nearly parallel to B

This is the case in the Time Projection Chamber (TPC). Assuming E along z and the components  $|B_x|$  and  $|B_y| << |B_z|$ , one finds in first order

$$u_x/u_z = (-\omega \tau B_y/B_z + \omega^2 \tau^2 B_x/B_z) / (1+\omega^2 \tau^2)$$
 (2.28)

$$u_v/u_z = (\omega \tau B_x/B_z + \omega^2 \tau^2 B_v/B_z) / (1 + \omega^2 \tau^2)$$
 (2.29)

In a TPC this will produce a displacement after a drift length L of  $\delta_x = L u_x/u_z$  and  $\delta_v = L u_v/u_z$ . As example, let us assume  $B_x = 0$  and  $\omega \tau >>1$ . Then  $u_v/u_z \sim B_v/B_z$ . A good alignment

of the E and B axes is therefore important to keep necessary corrections low. From measurements with both B-field polarities and different field strengths, the remaining  $B_x$ ,  $B_y$  can be determined, as well as  $\tau$ .

If  $B_x$  and  $B_y$  are small with respect to  $B_z$ ,  $u_z$  remains unaffected by B.

#### 2.2.2. Diffusion

For a long time, diffusion in gases without magnetic fields has been assumed to be isotropic. In 1967, however, it was found experimentally [29], that the *longitudinal diffusion*  $D_L$  for electrons along E can be significantly different from the *transversal diffusion*  $D_T$ . Subsequently it has been established that this is usually the case for electrons [33].

To achieve high precision in calculations of diffusion coefficients, the use of Monte Carlo techniques [11] or a multiterm expansion treatment of the Boltzmann equation [22] is even more important than for calculations of drift velocities. Errors introduced by a 2-term treatment were found to be around 5% for electron diffusion in nitrogen.

### 2.2.2.1 Isotropic Diffusion

The simpler case of isotropic diffusion shall be treated first. It describes well the behaviour of ions, except for very large electric fields E, and is a reasonable approximation for electrons in some cases.

Due to the random collisions with the gas molecules, a pointlike cloud of electrons or ions starting at t=0 to drift in the z-direction due to E will at time t show a Gaussian density distribution

$$N = (4\pi D t)^{-3/2} \exp(-r^2 / (4Dt)), \qquad (2.30)$$

with  $r^2 = x^2 + y^2 + (z-ut)^2$ , D being the diffusion coefficient. In any direction from the cloud centre, the mean squared deviation of the electrons is

$$\sigma_{x} = (2D t)^{1/2}.$$
 (2.31)

D is usually determined from the variation of the lateral cloud width as function of z = t u

$$\sigma_{\rm v}^2 = 2D \, z / u.$$
 (2.32)

Related to the diffusion coefficient D is the diffusion constant  $D^*$ , with

$$D^{*2} = 2D / u, (2.33)$$

leading to

$$\sigma_{x} = D^{*} z^{1/2}$$
. (2.34)

The diffusion constant  $D^*$  is the diffusion spread for a single electron after 1 cm drift. For a drift length L cm the spread will be  $\sigma_x = D^* \sqrt{L}$ .

In terms of the microscopic picture, D is given by

$$D = \lambda^2 / (3\tau) = v\lambda / 3 = v^2 \tau / 3 = (2/3)(\varepsilon / m) \tau, \qquad (2.35)$$

with  $\lambda$  being the mean free path,  $\lambda = v\tau$ , and  $\varepsilon$  the mean energy.

As  $u = (eE/m) \tau = \mu E$ , with  $u = drift velocity and <math>\mu = mobility$ ,

$$\varepsilon = (3/2) (D/\mu) e$$
 . (2.36)

The mean energy  $\varepsilon$  can be determined by a measurement of D and u.

Instead of  $\varepsilon$ , one often finds the 'characteristic energy'

$$\varepsilon_k = (2/3) \,\varepsilon = e \,D / \mu. \tag{2.37}$$

The lateral diffusion width  $\sigma_x$  after a drift distance L can also be expressed in terms of the mean energy  $\varepsilon$ :

$$\sigma_x^2 = 2Dt = 2DL / (\mu E) = (4/3) \varepsilon L / (eE).$$
 (2.38)

To obtain low diffusion and thus good spatial resolution in drift chambers, a low electron energy and high electric fields are required. The lower limit for  $\varepsilon$  is the thermal energy  $\varepsilon_{th} = (3/2)$  kT. In this limit, the relationship known as *Einstein or Nernst-Townsend formula* follows:

$$D/\mu = kT/e. \tag{2.39}$$

The minimum diffusion width is thus

$$\sigma_{x,min}^2 = (kT/e) (2L/E)$$
. (2.40)

As can be seen in figure 10, this minimum is approached for electrons in 'cold gases' like  $Ar/CO_2$  up to  $E \sim 100$  V/cm at 1atm, for 'hot gases' like  $Ar/CH_4$  only for much lower fields. Ions follow this thermal limit always, except in very high fields.

### 2.2.2.2 Anisotropic diffusion

For anisotropic diffusion in an electric field E along z, the transversal diffusion coefficient  $D_T$  is defined by

$$\sigma_{\rm x}^2 = 2D_{\rm T} t = 2D_{\rm T} L / u_{\rm z} ,$$
 (2.41)

 $\sigma_x^{\ 2}=2D_T\,t=2D_T\,L\,/\,u_z\ ,$  and the longitudinal diffusion coefficient  $D_L$  along E is by

$$\sigma_t^2 = u^{-2} \sigma_z^2 = 2D_L u_z^{-2} t = 2D_L L / u_z^3$$
 (2.42)

Measurements of lateral diffusion, drift velocity and spread of arrival times  $\sigma_t$  allow determination of both diffusion coefficients. To obtain precise results, great care has to be taken to measure single electrons with good efficiency [30].

#### - Magnetic field effects

A magnetic field B along z will curl up electrons in the x-y projection between collisions. The lateral diffusion will thus be reduced:

$$D_{T}(B) / D_{T}(0) = 1 / (1 + \omega^{2} \tau^{2}).$$
 (2.43)

This reduction is essential for most TPCs operating at 1 atm with their long drift distances. At higher pressure, the shortening of  $\tau$  reduces the gain.

A more rigorous treatment of averages [7] shows that at high B the ratio is changed to

$$D_{T}(B) / D_{T}(0) = 1/(C + \omega^{2} \tau_{2}^{2})$$
 with a different  $\tau$ . (2.44)

This behaviour was indeed verified [32], by measuring D(B) over a wide range of B [24]. In an Ar/CH<sub>4</sub> (91/9) mixture the data could be fitted with  $\tau$  = 40ps ,  $\tau_2$  = 27ps and C = 2.8. The low field behaviour is followed up to about 2 kG, the high field behaviour is approached above about 3.5 kG .

The *longitudinal diffusion* remains unchanged :  $D_L(B) = D_L(0)$ .

Figures 10-12 show transverse and longitudinal diffusion for a few drift chamber gases. A data base for many gas mixtures, calculated with Magboltz 2, vs.7.1 has been compiled in [33]. It contains diffusion coefficients as function of E and B ( for transverse diffusion only) and drift velocities as function of E. One example is shown in figure 11.

### 2.2.3 Electron attachment

Drifting electrons may be absorbed by electronegative components or impurities in the gas mixture. Halogenides (e.g. CF<sub>4</sub>) and oxygen have particularly strong electron affinities. Two-body and three-body attachment processes are distinguished [34].

In the *two-body process*, the molecule may or may not be broken up:

$$e^{-} + AX \rightarrow AX^{-*} \rightarrow A \text{ (or } A^{*}) + X^{-} \text{ (or } X^{-*}) \text{ or }$$
 (2.45)

$$e^- + AX \rightarrow AX^{-*} \rightarrow AX^- + \text{energy}$$
. (2.46)

The attachment rate R is proportional to the density N:

$$R = c \sigma N \tag{2.47}$$

for an electron velocity c and attachment cross-section  $\sigma$ . The rate constants of freons and many other halogen-containing compounds are known [35].

The Bloch-Bradbury process is the best known three-body process [36]: an electron is attached to a molecule through the stabilizing action of another molecule. This process is important in  $O_2$  for the attachment of electrons with energies below 1 eV, forming an excited unstable state with a lifetime  $\tau$  of the order of  $10^{-10}$  s. A stable ion will be formed only if the excitation energy is carried away during  $\tau$  by another molecule. As the attachment rate depends on the product of the concentrations of oxygen and of the stabilizing molecules, it is proportional to the square of the gas pressure [7]:

$$R = \tau c_e c_2 \sigma_1 \sigma_2 N(O_2) N(X) . \qquad (2.48)$$

Here  $c_e$  is the electron velocity,  $c_2$  the relative thermal velocity between  $O_2$  and X. An  $O_2$  contamination of 1 ppm in an Ar/CH<sub>4</sub> (80/20) mixture at 8.5 atm causes an electron absorption of 3% / m at a drift speed of 6 cm /  $\mu$ s.

### 2.3. Signal formation

All TPCs operated in experiments have so far used Multiwire Proportional Chambers (MWPC) for the readout. Presently, for the first time, a TPC with a different readout is installed in an experiment at T2K (see section 3.6.2). We shall, therefore, first discuss the MWPCs. The signal is determined by induction from the moving charges, the gas amplification near the anode wire and the response of the electronics. The shaping times in the MWPC have to be between 100 and 200ns typically. This results in a noise of at best some 300 but often >1000 electrons. In addition, only a fraction of the total ionization is normally available with this pulse shaping (see 2.3.1.) For this reason, a gas amplification of > 10000 is usually required. This amplification is obtained by avalanche multiplication of the original electron in the high electric field of up to E ~ 200 kV/cm around the thin anode wire (diameter ~20  $\mu$ m) at 1atm.

#### 2.3.1. Signal induction

We shall consider the simple case of a single anode wire on the axis of a cylindrical cathode tube. This describes well the general situation in a MWPC, because inside about 1mm around the anode wires the field is radial and almost all electrons are produced closer than  $100\mu$ m to the wire [37].

Signals are always produced by induction from the moving charges.

In any electrode configuration, the current I<sub>R</sub> induced on the readout electrode R is given by

$$I_{R} = -q \mathbf{E}_{\mathbf{w}} \bullet \mathbf{v} , \qquad (2.49)$$

where q is the signed charge moving with the vectorial velocity  $\mathbf{v}$  and  $\mathbf{E}_{\mathbf{W}}$  is a vectorial 'weighting field', a conceptual field defined by applying +1V on R and 0V on all other electrodes. The unit of  $E_{\mathbf{W}}$  is 1/cm [38, 39].

The actual v is calculated by applying the normal operation voltages, including possibly a B field. In the special case of a two electrode system like the wire tube or a parallel plate chamber,  $E_w = E_{op} / V$ , where  $E_{op}$  is the actual operating field obtained with the voltage V on R (the anode wire) and zero V on the cathode.

For the proportional tube with wire radius a and cathode radius b,  $E_{op}$  and  $E_{W}$  are obviously radial with

$$E_{op} = V / [r \ln(b/a)]$$
 (2.50)

 $E_{op}\!=V\,/\,[\,\,r\,\ln(b/a)]\quad.$  We assume constant mobility  $\mu$  for the positive ions. Therefore

$$v^{+}(t) = \mu V/[r(t) \ln(b/a)]$$
 (2.51)

For a positive ion starting at t = 0 from  $r = r_1$ ,

$$r(t) = r_1 (1 + (t/t_0))^{1/2}$$
 with  $t_0 = r_1^2 \ln(b/a) / (2\mu V)$ . (2.52)

The maximum time for an ion to drift from a to b is

$$T^{+}_{max} = (b/a)^{2} t_{0}$$
, as  $(b/a)^{2} >>1$ . (2.53)

The induced current I<sup>+</sup> is

$$I^{+} = -q \mathbf{E}_{\mathbf{W}} \bullet \mathbf{v}^{+} < 0 \quad , \tag{2.54}$$

as  $\mathbf{v}^{+}$  is parallel to  $\mathbf{E}$ .

For the integrated charge Q, one gets

$$Q^{+}(t) = \int I \, dt = \int I \, (1/v^{+}) \, dr = \int -q \, E_{w} \, dr \quad . \tag{2.55}$$

Integration from  $r_1$  to  $r_2$  gives

$$Q_{1\to 2}^+ = -q \ln(r_2/r_1) / \ln(b/a), \text{ with } q > 0 \text{ and } r_2 > r_1.$$
 (2.56)

For an electron one obtains

$$Q_{1\to 2}^{-} = + q \left| \ln(r_2/r_1) \right| / \ln(b/a), \text{ with } q < 0 \text{ and } r_2 < r_1,$$
 (2.57)

as v is antiparallel to  $E_{\boldsymbol{w}}$  .

We shall give numbers for a typical proportional tube, assuming:

a = 10  $\mu$ m, b = 2.5 mm,  $E_{op}$  (r = a) = 200 kV/cm,  $\mu^+$  = 1.9 atm cm² / (Vs), v² > 5 10<sup>6</sup> cm/s and to estimate the gas amplification A, the Diethorn parametrization  $\alpha = (ln2 / \Delta V) \, E$  and  $E_{min} = V / (r_{min} ln(b/a))$ . For an Ar/CH<sub>4</sub> (90/10) mixture,  $\Delta V = 23.6 \, V$  and  $E_{min} = 48 \, kV/cm$  is assumed [7, p.136]. Here  $r_{min}$  is the starting radius for the avalanche and  $E_{min}$  the minimum field permitting multiplication.

We obtain :  $t_0 = 1.3$  ns,  $T^+_{max} = 82 \ \mu s$  ,  $r_{min} = 42 \ \mu m$ , A = 4400 .

The last electron will be collected in a very short time of about 0.6 ns, the vast majority even faster. Half of the electrons move only about  $2\mu$ m, the next 25% some 4  $\mu$ m and so on. A rough estimate of the induced electron charge signal is, therefore,

$$Q_{\text{total}} = q \ln(14/10) / \ln(2500/10) = 0.06 \text{ q} . \tag{2.58}$$

Only about 6% of the total induced signal is due to the movement of the electrons, the rest comes from the ions, if one integrates over the full ion collection time,  $82 \mu s$ . In practice, however, one mostly uses much faster integration. The long tail in the signal caused by the very slow ion movement has to be corrected for by electronic pulse shaping to avoid pile-up at high rates. If one uses fast pulse shaping, say 20ns integration time, only a fraction of the ion charge will be seen: an ion starting at  $r_1 = a$ , reaches  $r_2 = 40 \mu m$  in 20 ns and induces about 25% of its charge. That means: with 20 ns pulse shaping, one may expect to see an *effective charge* of about 30% of the total charge produced, of which one fifth is due to the electrons.

At higher pressure p, the same gas amplification is obtained for a lower E/p. As a consequence, ion drift is slower and therefore also the signal formation.

### 2.3.2. Gas amplification

In high enough electric fields, the number n of electrons will grow on a path ds by

$$dn = n \alpha ds, \qquad (2.59)$$

where  $\alpha$  is the 'first Townsend coefficient'. As the ionization growth is proportional to the gas density  $\rho$  and the ionization cross-section depends on the instantaneous energy  $\varepsilon$  of the electrons, which is dependent only on  $E/\rho$ ,  $\alpha/\rho$  is given usually as function of  $E/\rho$ . Some examples of measurements [40] and Monte Carlo simulation are shown in figure 13. In the region of interest to gas detectors, up to about 250kV/cm,  $\alpha$  rises fast with electric field. The agreement between measurements and calculation is reasonable for the lower field values. The difference at the highest fields is attributed to the fact that photo- and Penning –ionization has been neglected.

The amplification A in the detector is then

$$A = n / n_0 = \exp \int \alpha(s) ds = \exp \int \alpha(E) dE / (dE/ds), \qquad (2.60)$$

if  $n_0$  is the initial number of electrons, e.g. from a track segment.

In the amplification region near the wire, the field is

$$E(r) = q_s / (2\pi r \varepsilon_0), \qquad (2.61)$$

where q<sub>s</sub> is the charge per cm. Therefore,

$$A = \exp \int q_s \alpha(E) dE / (2\pi\epsilon_0 E^2) . \qquad (2.62)$$

Two approximations in particular have been used to describe practical cases.

The early *Korff model* [42] uses the parameterization

$$\alpha/p = A \exp(-Bp/E),$$
 (2.63)

with empirical constants A and B depending on the gas.

In the *Diethorn approximation* [43],  $\alpha$  is assumed to be proportional to E. One then obtains for a proportional tube with wire radius a and tube radius b

$$\ln A = (\ln 2/\ln(b/a)) (V/\Delta V) \ln (V/(\ln(b/a)) a E_{\min}),$$
 (2.64)

where the two parameters  $E_{min}$  and  $\Delta V$  are obtained from measurements of A at various voltages and gas pressures.  $E_{min}$  is the minimum E field to start the avalanche and  $e\Delta V$  the average energy required to produce one electron. A list for  $E_{min}$  and  $\Delta V$  for various gases is given e.g. in [7]. As  $E_{min}$  is defined for a density  $\rho_0$  at STP,  $E_{min}(\rho) = E_{min}(\rho_0)$  ( $\rho/\rho_0$ ). Reasonable agreement with the experimental data is obtained; discrepancies show up at high A.

The amplification  $A=n/n_0$  is the mean of a Gaussian distribution with variance  $S^2$ . If  $n_0 >> 1$  and if all  $n_0$  avalanches develop independently,  $S^2 = n_0$   $\sigma^2$ , where  $\sigma^2$  is the variance of the probability function P(j) for producing an avalanche of j electrons starting from one, if the mean is A. Distributions for single electron amplification derived theoretically [44] and measured [45] for the strong inhomogeneous field around a thin wire approach Polya distributions, see figure 14. For these distributions

$$(\sigma_A / \langle A \rangle)^2 = f$$
, with  $f \le 1$ . (2.65)

The limiting case f=1 is an exponential distribution (Yule-Furry law)

$$P(A) = (1 / \langle A \rangle) e^{-A/\langle A \rangle}$$
 (2.66)

Experimental results point to f = 0.6-1.0. Measurements with laser tracks [7], indicate that the r.m.s. width  $\sigma_A$  of a single-electron avalanche is close to the mean, as it is for the exponential distribution. Another very careful measurement also favours an exponential distribution [24, 14], except for a sharp drop at very low pulse heights.

For a parallel plate geometry, calculations [46] agree well with measurements [47].

Besides avalanche fluctuations, many operational and geometrical parameters influence the gas amplification, amongst which are:

#### - Geometrical imperfections

The effects will obviously depend on the geometry and the operation details. An early publication [37] gives analytic estimates of the effects of wire displacements and variations in wire diameter. In a typical geometry  $dA/A \sim 2.5$  dr/r, where r is the wire radius;  $dA/A \sim 9$  dgap/gap.

#### - Edge effects

Near edges, the electric field is reduced over distances similar to the gap between the electrode planes. It can be recovered largely by additional field shaping lines on the edges [48].

#### - Gas density

The Diethorn approximation gives

 $dA/A = -(\ln 2/\ln(b/a))(V/\Delta V)(d\rho/\rho) = -(5-8)d\rho/\rho$  typically . Pressure dependence can be corrected for, as pressure is usually well measured.

- Space charge

Due to the low velocity of the positive ions (falling off as 1/r from > 1 mm/ $\mu$ s at r=a), space charge will build up at high particle fluxes and reduce the avalanche amplification. In drift tubes, the voltage drop due to the space charge from a given particle flux is proportional to the third power of the tube radius. A smaller radius thus improves the rate capability drastically.

#### **2.4.** Calibration with laser beams

The development of TPCs and other detectors with long drift distances triggered the interest in using laser beams for calibration. They should offer several advantages: stable position in space, insensitivity to magnetic fields, no multiple scattering, narrow pulse height distribution even on short track segments without  $\delta$ -electrons and easy ways to produce well defined multiple tracks. The problem was that single photon excitation had to be excluded. Lasers in the vacuum UV are impractical and the photon energies of available lasers in the near UV, e.g. N<sub>2</sub>-lasers (hv = 3.67 eV) or quadrupled Nd-Yag lasers (hv = 4.68 eV), are too low to directly ionize even the lowest ionization potentials IP of complex molecules.

The first successful double photon ionization was obtained with a  $N_2$ -laser with nickelocene (IP = 6.5 eV) as additive [49]. Soon two independent studies showed that significant ionization could be produced even in undoped gases on impurities [50, 51]. A detailed interpretation was given [50], also for the fact that sometimes a linear dependence of signal versus laser intensity was observed, assuming saturation of the first step. It was demonstrated that with a special laser construction for low beam divergence sufficient ionization is obtained over long distances [51].

These first results triggered a large number of studies. Many additives were shown to be ionized with the  $N_2$ -laser and even more with the higher photon energy of a quadrupled Nd-Yag laser ( $h\nu = 4.68 \text{ eV}$ ). Although traces of many possible candidates for two-photon ionization were detected in samples of gases from drift chambers, the impurities responsible for the signals in 'undoped' chambers remained unknown, except in two cases, where phenol and toluene were found to contribute [52, 53]. An account of the vast amount of studies may be found in two reviews [55, 56].

It turned out, as a great surprise, that adequate signals could be detected in basically all undoped chambers, with good stability over long times. It was even difficult to suppress laser ionization completely in very clean systems [54]. Therefore, operation of both TPCs and of the Jet Chamber at LEP was started tentatively with undoped gas mixtures. It was found that the signals remained acceptable without additives over the whole operation period of a decade, even with the lower photon energy of the N<sub>2</sub>-lasers in DELPHI. An example of reconstructed laser tracks in ALEPH is shown in Fig. 15. The most recent two large TPCs for STAR and ALICE have both installed very complex systems [57, 58] and installation is foreseen for the T2K TPCs. STAR is using a system of 500 beams to monitor drift velocity to 0.02% and to correct various ExB corrections and is relying strongly on them for measurements of space charge effects, especially at the higher RHIC luminosities.

The spatial stability of the laser beam can be about  $100 \mu m$ ; with only 100 shots, the mean position is thus defined to  $10 \mu m$ . Besides their use in large chambers, laser beams have also found applications in numerous small-scale studies of drift chamber performance.

### 2.5. Ageing of wire chambers

Since the invention of gaseous detectors ageing has been observed. It has become one of the major concerns in recent experiments, because of the enormous radiation dose detectors have to stand. Amongst the effects of *ageing* are: decreasing signal, broadening energy resolution and increasing dark currents, finally electric breakdown or even broken wires. Several reviews [59] and workshop proceedings [60] give a detailed account of the immense number of studies of this subject.

As causes of the ageing effects, deposits have been found on sense wires and cathodes. Any form from smooth layers to long whiskers has been observed on the anode wires [61], see figure 16. On cathodes, thin insulating spots are usually found in discharge areas, representing signs of a Malter effect [62]: under irradiation charges build up until their field extracts electrons from the cathode through the insulator into the gas, where they initiate new avalanches. Delays of the charging-up shortening with higher irradiation rate and slow decay after irradiation is stopped support this assumption. Addition of small amounts of alcohol or water vapour have sometimes reduced the effect, probably by providing some conductivity. Analysis of the deposits often indicated carbon compounds and also Si, more rarely other elements: Cl, O, S.

The drop in pulse height A often follows the integrated charge load in Coulomb per cm wire, independent of radiation rate, but occasionally some rate dependence has been observed. Very crudely, classical gas mixtures containing hydrocarbons have shown ageing rates of

- $-\Delta A / A \sim (0.01 0.1) \% / mC / cm$  for small detectors,
- $\Delta$  A / A ~ (0.1-1) % / mC / cm for large detectors.

Many qualitative explanations have been proposed for specific cases of ageing but there exists no quantitative explanation. On the other hand, the studies permit the formulation of some *general rules* for increasing the chance for a longer detector survival:

Hydrocarbons (Methane, Ethane etc.), very often used in the past, should be avoided for the highest radiation levels. For these, only a very restricted list of suitable gases remains: mixtures of rare gases and  $CO_2$  and possibly  $N_2$ ,  $CF_4$  or DME.  $CF_4$  offers high electron drift velocities and has proven to be capable under certain conditions to avoid formation of or even to etch away deposits, in particular in the presence of minute Si impurities. But its aggressive radicals can also etch chamber components, especially glass [63]. In any case, the water content has to be kept below 0.1%, if  $CF_4$  is used, to avoid etching even of goldplated wires. Also DME, offering low diffusion, has in some cases provided long lifetime. It was, however, proven to attack Kapton and to be very sensitive to traces of halogen pollutants at the ppb level.

- Many materials have to be avoided [59e], in the gas system, in the detector and during the construction: Si compounds, e.g. in bubbler oils, adhesives, vacuum grease or protection foils, PVC tubing, soft plastics in general, certain glues and many more. Details can be found in the workshop proceedings and reviews mentioned, also on suitable materials.
- *High cleanliness* has to be observed during construction e.g. to avoid resistive spots on the cathodes. The sense wire has to be continuously checked during wiring to assure the required quality of its geometrical tolerances and of the gold plating.
- Great effort should go into the electronics to allow the *lowest gas amplification* possible.
- A *final detector module* with the final gas system components should be *extensively tested* under irradiation *before 'mass production'*. Last minute changes have often caused problems. As an accelerated test over typically <1 year is usually required for practical reasons, to obtain the full integrated charge for some 10 years of operation, an uncertainty will unfortunately remain, because a rate dependence of the ageing can not be excluded.
- TPCs are meant to see significantly lower particle rates and thus less integrated charge per cm of anode wire than other high-rate detectors at LHC, as already dictated by the long drift length and resulting space charge and event reconstruction problems. Nevertheless, the beforementioned precautions are obligatory in most experiments, because radiation hardness can be deteriorated by orders of magnitude e.g. by inadequate choice of materials or construction procedures.

#### 3. TPC Characteristics

Tables 4a and 4b summarize properties and performance of some TPCs.

### 3.1. Basic design - PEP 4 TPC

The TPC is basically a long drift chamber with parallel electric and magnetic fields and 3-D points read-out at the end(s). The design principles shall be explained by taking the example of the PEP4 TPC, not only because this was the original TPC but also because the choices taken at that time were based on studies of many of the options, which have again been considered in later developments.

The design of the PEP4 TPC proposal is sketched in figure 17. Developed for operation at an electron-positron collider, it is in the form of a double cylinder around the beam pipe, 2m long, centered on the interaction point and inside a solenoid. A central high voltage plane (on negative potential) supplies the field for drifting electrons towards the two readout planes, one at each end; the drift length is 1m. An inner and an outer field cage terminate the drift volume radially (radius = 20 cm and 100 cm, resp.) and define a homogeneous drift field. Each end-cap has the MWPC arranged as 6 sectors, each with 183 'azimuthal' anode wires. Fig.18 shows three cuts through the MWPC. The wire plane terminating the drift volume acts as a gating grid. This grid was actually only added for the second run period, because space charge problems due to background had turned out bigger than anticipated. When the gate is 'open', the electrons drift through it and also through the second grid, which acts as one of the cathodes of the MWPC. Avalanches are initiated near the anode wires (diameter =  $20 \mu m$ ). The anode wires ( $20 \mu m$ ) have a pitch of 4mm and alternate with field wires (75  $\mu$ m). The field wires were considered important to reduce the crosstalk between the anode wires, as their pulse heights are used to provide particle identification through ionization sampling. The other cathode is formed by a printed circuit board, segmented into equidistant rows of (7.5 x 7.5) mm<sup>2</sup> pads below 15 of the sense wires. The number of pad rows was limited by space for the pre-amplifiers on the sectors and cost of the read-out. Centroid calculation of the pad pulse heights provides precise r-φ information along the wire. The signals from all anode wires and cathode pads are sampled at 10 MHz with CCDs, which provide z-information (along the drift direction). The CCDs accept 455 analog samples and are read out at about 20 kHz. For a track traversing the full radius, there are thus 15 points measured with 3-D information and 183 dE / dx samples for particle identification.

A high pressure of 10 atm was specified to optimize particle identification with a compact design. An Ar / CH<sub>4</sub> (80/20) mixture was chosen, because of low electron attachment and chiefly because of the high drift velocity u at low field E, due to the Ramsauer dip in the cross-section. These two characteristics are especially important at high pressure to avoid higher electric fields and electron attachment from oxygen impurities, which increases with the square of the pressure. The original proposal foresaw operation at p = 10 atm, E = 0.2 V/cm/Torr and 15 kG. Measurements of the transverse diffusion of single electrons as a function of E had been carried out at 600Torr with 15cm drift in various gases, in magnetic fields up to 20.4 kG, see figure 12. From these measurements,  $\omega \tau \sim 10$  was obtained at 600 Torr for 20.4 kG. This permitted an estimate of the r- $\phi$  smearing due to transverse diffusion for a 1m drift in 15 kG at 10 atm of about 1.2 mm rms for a single electron. Assuming 160 electrons, i.e. the most probable number for a 4 mm sample, contribute to the signal, the measurement error due to diffusion was estimated as  $\sigma_D < 100 \ \mu m$  (a very conservative estimate for the effective number of 50 would lead to  $\sigma_D = 170 \ \mu m$ ). The specification of an average resolution of 200  $\mu m$ /point was, therefore,

considered conservative and used to estimate the momentum resolution to about  $\delta p/p = 0.6 \text{ p}\%$  for p > 1 Gev/c, well adapted to the PEP energies.

Initial space charge effects became negligible after the installation of the gating grids. Distortions due to charging up of the field cages were strongly reduced by a reduction of the non-conducting sections and by the application of a surface coating. With the final field of 13.25 kG at 8.5 atm, an average point resolution of 150  $\mu$ m was achieved, the best of all large TPCs. The momentum resolution, however, remained somewhat worse than expected with about 1.0 p%, for reasons only partially understood [64].

It is interesting to note that for the same gas and E-field, at 1 atm a field of 15 kG along the drift direction reduces the single electron diffusion  $\sigma_{D,1e}$  from about 4130 to  $700\mu m$ , a value below that for 10 atm, because of an  $\omega \tau = 5.8$  at 1 atm, compared to  $\omega \tau = 0.58$  at 10atm. It is because of the higher effective number of contributing electrons that the higher pressure results in a smaller error in the measurement of the mean.

Excellent particle identification was achieved with a resolution of 3.0% for minimum ionizing particles and 2.7% for Bhabha electrons, the best value of any TPC to date [64].

### **3.2.** Specific aspects

### 3.2.1 Wire Chamber layout

Several parameters in the wire chamber layout may be varied to adapt to particular priorities: use of field wires, gap sizes, wire pitch and sector boundary design. Figure 18 shows the layout chosen by PEP4.

#### *3.2.1.1. Field wires*

The PEP4 TPC used field wires to reduce crosstalk between the anode wires and thus corrections to the dE/dx samples taken from them. Most TPCs followed this choice. The argument drops of course when the anode wires are no more read out, as in STAR and ALICE, because of the extreme occupancy. Dropping field wires brings the advantage of a higher percentage of the induced charges on the pads. In the ALEPH geometry, with 4mm gaps (anodecathode) and 4mm anode wire pitch, pads receive about 20% of the anode charge with the field wires (which get about 40%) and would receive about 35% without them [66]. In the inner sectors of STAR even > 40% is received by the pads, because of the small anode-cathode gap of 2 mm.

Dropping the field wires avoids problems from corona discharges on the frames, where anode and field wires are soldered. This was actually considered the major argument against adding field wires.

On the other hand, operation without field wires demands a higher voltage on the anode wires for the same gas amplification.

#### 3.2.1.2. Pads

The PEP 4 TPC and most later TPCs have straight pad rows. As track angles not normal to the pad row cause an additional error for the spatial resolution, ALEPH and DELPHI have chosen circular pad rows in the cylindrical geometry of a collider. The choice of the size of the pads depends on many parameters including cost. The width along the pad row, i.e. along r-φ, is usually smaller than the length. ALEPH decided for longer pads to improve resolution for the highest momenta, DELPHI for short pads to improve performance for tracks from secondary vertices. The effect of the length on spatial resolution is complex, see below. For best space resolution, the ratio 'pad-width / gap (anode-cathode)' should be about 1-2 [121, 122]. For larger ratios, precision is lost for tracks passing above the centre of a pad. For lower ratios, the precision is limited by the lower signal-to-noise ratio. To reduce occupancy, STAR and ALICE chose

thinner pads (2.85 mm and 4 mm, resp.) for the inner circle of sectors and NA49 for the Veretx TPC (3.5 mm).

### 3.2.1.3. *Gaps and wire pitch*

The gap (anode-pad) has been chosen as 4mm for most TPCs, but smaller for some: 3 mm for CERES, NA49 and ALICE outer chambers, even only 2 mm for the inner chambers of STAR and ALICE, matching their smaller pad width.

A pitch of the anode wires of 4 mm has been used in almost all TPCs, as it provides operational stability and a reasonable width for the dE/dx samples. An exception is made again by the inner ALICE chambers with a pitch of 2.5 mm (without field wires), matching the thin gaps.

The pitch of the cathode and gating grids is 1 or 2 mm. The 1mm grids show smaller ExB effects on the spatial resolution but exert larger forces on the frames. For the gating grid, a 1mm pitch brings the obvious advantage of lower gating voltage.

#### 3.2.2. Sector boundaries.

The sector boundaries formed by the frames supporting the wire planes represent dead zones in the endcaps. A higher number of sectors per  $2\pi$  results in more dead zones but smaller track angle errors for the r- $\varphi$  measurement. Larger TPC radii demand more sectors per  $2\pi$  to remain with stable wire length. One has to choose between full insensitivity for certain  $\varphi$ -segments, using the same radial boundaries over the full radius (eg PEP4, DELPHI (6 sectors /  $2\pi$ ), STAR (12), ALICE(18) or reduced sensitivity over larger  $\varphi$ -segments, by either using boundaries with steps along r- $\varphi$  (already discussed for PEP4 but not implemented) or by rotating in  $\varphi$  a second outer circle of sectors with respect to the inner one (eg ALEPH).

In addition to complete loss of information along the boundaries there is a serious loss inside the sensitive zone due to a reduction of gas amplification over more than a cm near the boundaries. Figure 19 shows an early measurement of this effect and also the corrective measure [48]. Additional guard strips on the wire support frames on a suitable potential can recover some 8mm with full gain.

### **3.2.3.** Gating

Because of their long drift length, TPCs are particularly prone to space charge effects. For the PEP4 TPC it was estimated that a charge deposition of 10GeV/s, equivalent to 5000 m tracks/s would cause detectable field distortions. Background turning out higher than expected, a gating grid had to be added. Most later TPCs used a similar geometry, see figure 20. A grid with wires stretched parallel to the anode wires with a pitch of 1-2mm is mounted 4-8 mm above the shielding grid. To close the gate, a differential potential  $V = V_G \pm \Delta V$  is applied to alternating wires. For the ALEPH specifications (Ar/CH<sub>4</sub> at 1atm) the following results were obtained [67]. A gating grid with 1 (2) mm wire pitch is fully transparent for a V<sub>G</sub>, which produces a field between the gating grid and the cathode about twice the value of the main drift field. The gate is closed for the ions with  $\Delta V = \pm 20$  (40) V, both without magnetic field B and with B = 1.5 T. For electrons, it is also closed for B = 0, but it opens when the field is raised. For B = 1.5 T,  $\Delta V$  =  $\pm$  190 V is required for a grid with 2 mm pitch. At  $\Delta V = \pm 40 V$ , the transparency for electrons is about 75%. The big difference in the behaviour of ions and electrons in a strong magnetic field stems from the fact that in the gas mixture used  $\omega \tau >> 1$  for electrons and  $\omega \tau << 1$  for ions. Electrons, therefore, follow closely the magnetic field lines, whilst ions follow mainly the electric field lines.

The gating behaviour was measured without magnetic field also at 8.5atm in Ar/CH<sub>4</sub> [68]. A gate with 1mm pitch showed full transparency for a field between cathode and gating grid equal to 1.9 times the drift field. The gate was closed for  $\Delta V = \pm 100 \text{ V}$ .

The gate may be used in different ways. The simplest is the *static mode*, which blocks all ions but lets most of the electrons pass, with a signal loss of about 25%. DELPHI found this acceptable for operation at LEP. In the second mode, *opening on a trigger*, the gate is normally closed but opens for the full drift time for a triggered event. This mode is used in the vast majority of TPCs and is foreseen for ALICE. Depending on the speed of the trigger decision and switching, the information of a small part of the drift volume is lost; in the case of the STAR trigger, opening take  $2.1 \mu s$ , resulting in 12 cm lost of the 2.1 m drift length. This loss is avoided in the *synchronous mode*, in which the gate is opened shortly before each bunch crossing and closed after a negative trigger decision or left open for the electron drift time after a positive trigger. ALEPH applied this mode at LEP, where the spacing of bunch crossings was  $22 \mu sec$ .

The TRIUMF TPC used a different gate arrangement. Each of the anode wires is mounted with its pad row inside a rectangular cathode, sampling the track ionization through a 6 mm slot. Above each slot are mounted two grids (wire pitch 0.6 mm) 1.6 mm apart. The gate is normally closed, and opened within 200 ns on a trigger. The opening is achieved by applying -48 V on the outside grid and +3 V on the grid nearer to the anode. The dual grid has a transparency of 90 % and deteriorates the spatial resolution by about 15 %.

### 3.2.4. Field cages

The field cages have to provide a very homogeneous electric field parallel to the magnetic field axis. Their construction is complicated by conflicting requirements: high mechanical and electrical precision and stability of geometry and alignment with the cathode and the MWPC on the one hand, minimized material and thickness on the other hand. Depending on the drift length and gas choice, voltages up to 100 kV are required. The basic principle is a linear voltage degrader composed of closely spaced parallel rings connected to a chain of high precision resistors. The cathode is connected to negative high voltage and the MWPC kept near ground potential.

For the insulation towards the outside two techniques are employed, using either a solid or a gaseous insulator.

The solid insulator can be much thinner geometrically, allowing smaller detectors beyond the TPC. It usually results, however, in more material in terms of radiation length. One example of this type is the choice for ALEPH field cage, 4.4 m long and 3.8 m in diameter, see figure 21. It has a double layer of electrodes (35  $\mu$ m Cu) separated by a Kapton foil (75  $\mu$ m) on a 4 mm thick insulator, composed of 120 layers of mylar wound helically and glued together. An Aluminum honeycomb 16 mm thick and sandwiched between two 1mm Aluminum foils provides the self-supporting structure. The total thickness is 4.8 % of a radiation length.

An example of a field cage with gaseous insulator is the one of ALICE. The choice of a low mass gas mixture with Ne demands a very high voltage of 100 kV for the 2.5 m drift length to obtain an acceptable drift velocity, still only about half that of the more common Ar/CH<sub>4</sub> mixtures. The electric field is formed by 166 aluminized Mylar strips wound around 18 support rods connecting the central cathode plane with an end plate. One rod contains the chain of resistors (7.5 M $\Omega$ ) and clamps to fix the strips. The rods lie in line with the dead zones between the read-out chambers. They are clamped to the wall of a vessel containing CO<sub>2</sub> as gas insulator, 15 cm thick. Both walls of this vessel are built with Nomex honeycomb sandwiches with prepreg and Tedlar skins. The wall towards the drift volume has Al strips on both sides, connected to a separate voltage degrader chain and the other wall has a continuous 50  $\mu$ m Al foil on both sides and provides the ground termination.

In all designs, insulating surfaces have to be minimized, especially between the conducting strips, to avoid charging up effects and resulting field distortions. Such a problem on the initial PEP4 field cage was cured by covering it with a thin layer of polyurethane, thus providing some small conductivity. Excellent alignment with the central electrode and the read-out chambers is obviously important.

#### Central cathode

The central cathode for TPCs at colliders has to be thin, as it lies in the symmetry plane around the interaction point. It should be flat and not deform with time. Several designs have been used: stretched stainless steel mesh (TOPAZ), carbon-coated mylar foil (ALEPH), 25  $\mu$ m aluminized mylar (ALICE), 70  $\mu$ m carbon-loaded Kapton (STAR) and aluminum honeycomb sandwich (DELPHI). In STAR, the membrane is secured under tension to an outer support hoop, which is mounted on the outer field cage. The membrane has just a central hole to pass the inner field cage but without any mechanical coupling to it except for a single electrical connection. Narrow aluminum strips are attached to each side of the membrane to provide a target with low workfunction for the UV laser.

#### 3.2.5. Calibration

In addition to the usual calibration procedures of wire chambers during and after construction, regular calibration and monitoring during operation is required for optimum performance of a TPC. Various techniques have been used.

The electronics is calibrated by pulsing the grid wires (e.g. PEP4, TOPAZ and STAR) or the field wires (e.g. ALEPH and DELPHI) and recording the response of the wires and pads at various pulse heights to cover the dynamic range. This calibration is important for the r- $\phi$  and dE/dx measurements. It also provides relative timing inside a sector.

Radioactive sources in the endplanes were used in several TPCs (PEP4, TOPAZ, DELPHI): rods embedded in the endplane can be moved to provide a point source through small holes to each wire in the 'ON' position. Three such rods per sector define three absolute gain calibrations of the wire and its electronics as well as the slope and curvature of the gain along the wires.

Actual event tracks are used for relative sector to sector timing; the time of tracks passing through the amplification zone defines the zero time for the drift time measurement. Time association of hits on wires and pads gives the relative time offset between them.

Lasers have consistently been used to measure the drift velocity to a precision down to  $2x10^{-4}$ . Laser systems with from three beams per sector to a total of almost 500 beams in STAR have been implemented. They have also been of great help in the study of all kinds of distortions in the tracking due to space charges, insulator charging up on the field cages and misalignments.

### 3.2.6. Choice of gas mixture

There exists no universally 'ideal gas' for a TPC. The physics to be studied defines the layout and a number of conflicting requirements for the gas. The gas mixture has to be optimized for each particular case.

The PEP4 collaboration opted for a high pressure TPC to optimize dE/dx resolution in a compact detector. As mentioned before, an Ar/CH<sub>4</sub> mixture offered two advantages: a high drift velocity of electrons at low electric field and low electron attachment to oxygen impurity, which is proportional to the square of the pressure. The 80/20 mixture was preferred over the 90/10 and 95/5 mixtures because of a longer 'plateau' of stable operation. Prototype measurements had shown a length of 600, 400 and 230V, resp. for the three mixtures.

The two advantages mentioned and perhaps the fact that Ar/CH<sub>4</sub> had become well understood lead to the use of P20 (80/20 mixture) and P10 (90/10) in most later TPCs. P20 offers higher electron velocity but P10 a maximum of the drift velocity at lower electric field. Operation on the maximum is advantageous for stability reasons.

ALICE opted for Ne /  $CO_2$  /  $N_2$  (90/10/5). Neon was chosen for its low radiation length and hence low multiple scattering.  $CO_2$  replaces  $CH_4$  as quencher to avoid common wire chamber ageing, although it is not clear that the risk is high for the anticipated radiation loads. As  $CO_2$  is a weaker quencher than  $CH_4$ ,  $N_2$  is added to increase the stable gain limit. This ALICE mixture, however, requires an electric field several times higher than that required for P10 or P20 to achieve a similar drift velocity. As on the working point there is a steep dependence of the drift velocity on temperature, a very tight limit of  $\pm 0.1^\circ$  has been specified for the temperature control. Due to the lower Z, charged particles produce in Ne a factor of 2 less ionization than in Ar. The gas amplification has to be raised to about 20000 to achieve the same signal / noise ratio.

For the Linear Collider TPC projects various mixtures are under consideration. The toughest demand for the TPC is the point resolution < 140  $\mu$ m for drift lengths up to 2.5 m. The choice of the gas may depend on the read-out technique chosen but it is clear that low transverse diffusion in a high magnetic field of about 4 T will be an essential requirement. One of the candidates, the so-called T2K mixture (Ar / CF<sub>4</sub> / i-butane 95 / 3 / 2) offers a high drift velocity for electrons of 73  $\mu$ m/ns at a moderate 200 V/cm electric field, a relatively low longitudinal diffusion constant of 250  $\mu$ m /  $\sqrt{c}$ m and a large  $\omega \tau \sim 20$  at 5 T, reducing the transverse diffusion coefficient to  $\sim 20 \ \mu$ m /  $\sqrt{c}$ m. From the simulation results [25] one would in fact expect a rather similar performance from the 'standard' mixture Ar / CH<sub>4</sub>(80 / 20).

#### 3.2.7. Read-out electronics

The development of TPCs is intricately linked to developments in electronics. In particular, the implementation of typically several hundred analog samples on each channel requires special designs. The first TPC (PEP4) was made possible by the appearance on the market of Charge Coupled Devices (CCDs), which could be used as linear analog shift registers, with adequate performance and at acceptable cost for a system with about 16 000 read-out channels. We shall describe this system and the one from ALICE, as a recent design for about 500 000 channels.

#### PEP4 electronics

The PEP4 TPC demanded charge and timing information from both wires (for dE/dx) and cathode pads (for centroid finding) [69]. To reduce input capacitance and thereby noise, the preamplifiers are mounted on the backside of the TPC endplates inside the gas volume. Their signals are sent via 100 feet 50 Ohm coax cables to remote amplifier/shapers each of which drives a CCD. The CCD input is sampled and pushed through the 445 buckets at 10 MHz, memorizing a 44.5  $\mu$ s history of analog drift information. During readout, the clock is changed to 20 kHz and the outputs of the 16 000 channels are digitized (to 9 bits) in parallel. A threshold is set at about four times rms noise and only non-zero data are transferred to buffer memories and read to tape.

The preamplifiers are charge sensitive FET integrators of low noise (< 600 electrons rms on the pads and <1000 on the wires), low power dissipation (< 120 mW) and occupying only  $1.2 \text{ cm}^2$ , an achievement at that time. Pulse shaping was chosen as long as possible to improve the signal and reduce the noise (mainly from series noise in the preamplifier). On the other hand, for good reconstruction efficiency in jets, clean separation of tracks within  $1\mu$ s was demanded. This led to the choice of a peaking time of 250 ns. The shaper (1 RC differentiator and 5 RC integrators with the same time constant), delivered a response to a delta impulse close to a Gaussian. It also

provided pole-zero cancellation of the 5  $\mu$ s decay time of the preamplifier and partial correction of the 'ion tail', with a RC differentiator (0.4  $\mu$ s), keeping the amplitude below 4% of its peak value after 600 ns. The pulse is broadened by diffusion and track inclination. Because of the slow signal formation, the measured signal is only about one third of the total charge at 10 atm (about 60% at 1 atm) with 250 ns shaping time.

A sampling frequency of 10 MHz was chosen. This guarantees a good determination of the signal charge from the pulse area and of the time centroid calculated from some 5 samples, with small errors due to the asynchronous sampling phase, the trigger for the start of the sampling sequence being provided by other detectors. The threshold set after the digitizer corresponds to about 3-5% of the signal peak and its effect can be corrected for. With the electron drift velocity of 5 cm/ $\mu$ s finally used and a maximum drift length of 1 m, an event was fully contained in some 200 CCD buckets.

A powerful testing scheme was implemented to calibrate each of the stages from the preamplifier to the digitizers. Electronic gain could be monitored to better than 1%.

For a gas amplification of  $\leq 2000$ , the electronic noise was about 1% of the signal for a minimum ionizing particle, resulting in a contribution to the spatial resolution from the pads of  $60\mu m$ .

The group was proud to keep the mass construction cost to 114 \$/channel, the cost including overhead to 280 \$/channel.

#### ALICE electronics

For the construction of this system with about 560 000 channels and the detection of events with extremely high multiplicity, novel developments were required [70]. To handle high track densities, special attention has been given to excellent ion-tail cancellation and baseline subtraction.

Only pad signals are read out. They are transmitted via Kapton cables to front-end cards (FECs) located some 10 cm away in a structure mechanically decoupled from the TPC endplate. Each channel in the FEC consists of two parts: (a) an analog ASIC (PASA) with an amplifier and semi-Gaussian shaper and (b) a mixed-signal ASIC (ALTRO), including a 10-bit 25 MSPS ADC, baseline subtraction, a tail cancellation filter, zero suppression and a multi-event buffer. The shaping time is 190 ns FWHM, the sampling rate of the ADC 5-12 MHz. The power consumption of the whole FEC, including a board controller is < 100 mW per channel. This is less than what required by the PEP4 preamplifier alone and is one clear indication for the extraordinary progress of the electronics in the last 30 years.

The first component of the ALTRO chip is the Baseline Correction-1 to perform channel-to-channel gain equalization and to correct non-linearity and low-frequency baseline variations. The next processor is an 18bit, fixed-point arithmetic, third-order Tail Cancellation Filter (TCF), designed to suppress the ion-tail to less then 1 LSB from the baseline, within 1  $\mu$ s after the signal peak. With fully programmable coefficients, independent for each channel, the circuit can cancel a wide range of tail shapes and correct channel-channel fluctuations. The next block, the Baseline Correction-2 (BC 2), applies a correction based on a moving average of samples within an window and removes non-systematic perturbations of the baseline that are superimposed on the signal. At the output a Zero Suppression Unit discards all data below a programmable threshold, except for a programmable number of pre- and post-samples around each pulse. The output is sent to a memory with storage capacity of up to eight events of 1000 words.

Isolated cosmic ray events in a prototype were used to tune the parameters, employing the TCF to cancel the tail up to 3  $\mu$ s and the BC 2 to remove the long undershoot and a secondary spike after 25  $\mu$ s due to the acceleration of the positive ions near the grid wires. Figure 22 shows the impressive result obtained for a high-multiplicity cosmic ray event, showing the pulses before and after correction through the TCF and the BC 2.

Other specifications for the electronics are: dynamic range = 900:1; Crosstalk < 1%; Maximum readout rate: 200 Hz for Pb-Pb collisions with up to 700 Mbytes / event and 1 kHz for p-p collisions. An occupancy of up to 50% near the inner TPC radius should be handled.

The radiation load in the TPC is supposed to be relatively low: 1 krad + 10<sup>11</sup> neutrons/cm<sup>2</sup> over 10 years. Standard radiation-soft technologies have, therefore, been used. Special attention has, however, been paid to protection against damage from Single Event Upsets by applying redundancy and solutions to detect and cure possible upsets in the configuration of the programmable devices.

#### 3.4. Performance

#### 3.4.1. Spatial resolution

The avalanches on the anode wires induce pulses on the cathode pads below and the  $r\phi$  coordinate is obtained from the center-of-gravity determination of the pulse heights from adjacent pads.

### 3.4.1.1. Pad response

The charge distribution induced by a pointlike avalanche on an anode wire is called the intrinsic *pad response function (prf)*. It is determined by the geometry of the proportional chamber, especially the gap g (anode-cathode). When measured with pads, the prf also depends on the pad size [121]. In addition, there is a dependence on the actual avalanche geometry - how much the avalanche surrounds the wire – which determines the path of the positive ions to the various electrodes. This is normally neglected but simulations clearly show the effect [71] and also some measurements with the ALTRO chip in ALICE [70 b].

As an example, numbers for the PEP4 geometry are given: with an anode wire pitch of 4mm, a gap (anode-cathode) of 4 mm and a pad size of (7.5x7.5) mm<sup>2</sup>, the measured width of the intrinsic prf is  $\sigma'_{0} = 3.6$  mm.

For the many avalanches resulting from the track ionization, there are several effects broadening the distribution. The collaborations have used different parameterizations; we shall follow the one by ALEPH. The actual prf is described by

$$\sigma_{prf}^2 = \sigma_0^2 + \sigma_D^2 z + \sigma_\alpha^2 (tg\alpha - tg\psi)^2 + \sigma_\beta^2 tg^2\beta$$
, (3.1)

where  $\alpha$  and  $\beta$  are the angles between the track and the normal to the wires and the pad row, resp. and  $\psi$  is the angle describing the ExB effect in a magnetic field (see figure 23); z is the drift distance.

Although in most TPCs straight pad rows follow the wire orientation, we consider the general case, which includes the circular pad rows of ALEPH and DELPHI. This has the advantage to clearly separate different effects. The errors are added quadratically, as they are assumed independent.

- The first contribution contains the width of the intrinsic prf, in addition the error from noise and calibration.
- The second term describes the broadening due to diffusion.
- **E** x **B** effect. The third term has two origins. Due to the track angle  $\alpha$ , the avalanches are spread over a wire segment d tg $\alpha$ , if d is the pitch of the anode wires. In addition, there is a spread caused by ExB: near the gating and cathode grids and near the anode wire, the electrons do not drift parallel to the magnetic field [74]. The deviations are described by  $\psi$  such that d tg $\psi$  corresponds to the actual smearing along the wire due to the sum of all three deviations, see figure 24. It is this whole third term, which one tries to suppress by using readout techniques

without anode wires, see section 5. The effect could be reduced somewhat in a standard TPC by a smaller pitch of the anode wires and the wires of the cathode (which might even be replaced by a mesh) and of the gating grid. But there are limits set by electrostatic stability and mechanical forces. A strong ExB effect was observed for the first time in the TRIUMF TPC, because in the PEP4 TPC the effect was largely suppressed by the high pressure and the lower magnetic field during the early runs.

- The last term stems from the fact that several anode wires are contributing to the pad signals, each one giving a different centre-of-gravity. The smearing is proportional to the pad length. The error due to this term for stiff tracks is significantly reduced with circular pad rows.

The pad width w is usually chosen such that for the smallest prf width =  $\sigma'_0$ , two to three pads will have signals well above noise, which corresponds to a ratio w / g of about 1-2. In this case, the signal / noise ratio is near optimum [121] and it turns out that the prf is well approximated by a Gaussian with a  $\sigma$  close to the gap value g:

$$P_i(x) = C \exp(-(x-x_i)^2/2\sigma^2),$$
 (3.2)

where x is the position of an avalanche and  $x_i$  and  $P_i$  are the centre and pulseheight of the i-th pad, respectively [122, 123].

From three-pad clusters  $P_1$ ,  $P_2$  and  $P_3$ , the prf width is deduced:

$$(w/\sigma)^2 = \ln(P_2^2/P_1P_3).$$
 (3.3)

Measurements of clean high momentum tracks as function of drift length and track angles  $\alpha_w$  and  $\alpha_p$  permit separation of the various terms and confirm the functional dependence. The Lorentz angle was measured as  $\psi = 32^\circ$  in ALEPH with 1.5T.

#### 3.3.3.2. Resolution in ro

For the azimuthal coordinate resolution  $\sigma_{r\phi}$  one expects qualitatively the same dependence on drift distance and track angles as for the prf, although statistical effects have to be considered. In fact, a corresponding parameterization has been used by ALEPH [72].

$$\sigma_{r\phi}^2 = \sigma_0^2 + \sigma_D^2 z + \sigma_\alpha^2 (tg\alpha - tg\psi)^2 \cos^2\alpha + \sigma_\beta^2 tg^2\beta$$
 (3.4)

For stiff tracks, the angle  $\beta$  is close to zero,  $\alpha$  varies from -30° to + 30°. In a test setup,  $\sigma_0 \leq 80~\mu m$  was measured, including electronic noise, digitization and errors in the calibration. ALEPH measured for the transverse diffusion term:  $\sigma_D = 35~\mu m~\sqrt{z}$  at B=0 and  $5~\mu m~\sqrt{z}$  at B=1.5~T, with drift length z in cm. This agrees with expectations for 3 cm long pads, about 90 electrons per cm along the track and a transverse diffusion for single electrons of 600  $\mu m~\sqrt{z}$ . For the  $\alpha$ -term,  $\sigma_\alpha = d~/\sqrt{12N_{eff}} = (1.15mm)^2~/~N_{eff}$  is expected, where d is the anode wire pitch and  $N_{eff}$  is an effective number of electrons statistically contributing, taking into account the effects of clustering. The fact that for high momentum tracks no significant dependence of  $\sigma_{r\phi}$  on  $\alpha$  was observed, is explained with declustering by diffusion for the long drift distances and thus increased  $N_{eff}$ . This effect had been observed earlier [20], see 2.1.3. The angle dependence of the  $\beta$ -term as measured with tracks from hadronic  $Z^{\circ}$  decays is shown in figure 24. It gives  $\sigma_{\beta} = 2.3~mm$  and is the dominent contribution above a few degrees. For isolated tracks from leptonic  $Z^{\circ}$  decays an overall resolution of  $\sigma_{r\phi} = 173~\mu m$  has been obtained.

For the DELPHI TPC, the Lorentz angle is  $\psi = 34^{\circ}$  [73(b)]. The resulting dependence of the resolution on  $\alpha_w = \alpha$  is presented in figure 25. The minimum at  $\alpha = -34^{\circ}$  is just off-scale. The effect of  $\beta = \alpha_p$  is also shown, up to larger angles than in figure 24.

### 3.3.3. Longitudinal spatial resolution

The longitudinal (axial) position z of track points is calculated from a fit to a few time buckets. With increasing dip angle, the distribution of the arrival times of the electrons is

stretched significantly. This reduces the longitudinal resolution, as can be seen from the measurements by ALEPH [72], figure 24.

#### 3.4. Particle Identification – dE/dx

The principal idea of the TPC is the combination of tracking and particle identification (PID) in a single detector. As described in section 2.1.2, gas ionization by a particle depends only on its velocity and the square of the charge and not on its mass. Particle identification can, therefore, be achieved by simultaneously determining the particle momentum and its velocity from the ionization. In the present context, when using the term dE/dx, because this is commonly done, we always mean the localized ionization deposited near the track.

To understand the possibilities and problems of the dE/dx measurement, we look at the results from the PEP4 TPC [15, p. 298], figure 26. For particle separation, precise knowledge of two parts is required: the general dependence of dE / dx on the velocity and the ionization deposit along a specific track. The ionization loss drops as  $1/\beta^2$  for low  $\beta$ , goes through a minimum for  $\beta\gamma = 3$ -4, then rises logarithmically in  $\beta\gamma$  ('relativistic-rise' region) until it reaches a plateau. Particle identification is easy in the  $1/\beta^2$  part but difficult in the relativistic-rise region. The dE/dx curve and in particular the slope of the relativistic-rise region and the plateau depend mainly on the gas and its pressure but also on the method used to measure the ionization. This function has to be determined from fitting the dE/dx measurements for well-identified particles in different  $\beta\gamma$  regions, like Bhabha electrons, cosmic muons and minimum ionizing pions.

To measure the ionization loss of a particular track with reasonable precision, many samples have to be taken on the track. This problem was first considered in [75]. A detailed study based on the Photoabsorption Ionization model (PAI) [76] concluded that the ionization resolution was continuously improving with increasing number of samples for a given track length. This conclusion was obtained from a likelihood treatment of the samples for different masses. Although this method is considered to be the most precise in principle, most groups have used the simpler so-called 'truncated mean' method. Figure 27 shows on the left typical distributions [77], also called *straggling functions*, of the ionization loss in a sample of 7.5 mm in the ALICE gas: Ne / CO<sub>2</sub> / N<sub>2</sub> (90 / 10 / 5). The mean and the variance are ill-defined. A more reasonable description is given by the most probable ionization  $I_{mp}$  and the FWHM. The procedure most widely used is the calculation of a *truncated mean*, which we denote as I, as the mean of the lowest p% of the pulse heights. The cut reduces the effect of fluctuations due to the long tail. Values of p = 40 - 80 have been used. The spread of I,  $\sigma$ (I), is not very sensitive to p in this range. Figure 27 shows on the right the distributions for p = 65%, well described by a Gaussian.

Excellent agreement between experiment and theory is achieved, both for the straggling functions and the truncated means, but only after inclusion of diffusion (causing some correlation between adjacent samples) and amplification fluctuations [66]. Their effect on the straggling function is seen in figure 28. When treating different sample lengths x, because of different pad lengths or track angles, the naïve assumption of proportionality with x is incorrect, see figure 29, which shows calculated straggling functions for different sample lengths x in Argon. As these distributions are normalized to x, the mean loss  $<\Delta/x>$  is the same, but the most probable loss changes. That means that straggling functions cannot be scaled with a single parameter (e.g.  $I_{mp}$ ). It turns out, however, that a 2-parameter scaling is adequate [78].

The quality of PID is determined by the separation power D with
$$D = (I_A - I_B) / [\sigma(I_A) + \sigma(I_B)] / 2$$
(3.5)

i.e. the separation of particle types A and B expressed in number of standard deviations. For the PEP4 TPC, the best K-  $\pi$  separation obtained was about  $3 \sigma(I_{\pi})$  with  $\sigma(I_{\pi}) / I_{\pi} = 3.0\%$  for minimum ionizing pions [64]. Figure 30 shows for a number of gas mixtures the measured separation power at 15 GeV/c, obtained from the lowest 40% pulse heights from 64 samples of 4cm length [79]. The relativistic-rise at 1 atm is highest for noble gases, around 1.6-1.7 with respect to the minimum dE/dx. The low-Z molecular gases show better resolution  $\sigma(I)$  but have a lower relativistic-rise. There is no 'magic gas' with outstanding PID properties in all respects, although there are significant differences. For the choice of gas in a particular experiment, other characteristics like diffusion, drift velocity and radiation length will enter, in addition to PID.

For rough estimates of the relative truncated mean resolution  $\sigma(I)/I$  as function of pressure p, sample size d and number N of samples in mixtures of Ar with 10-20% CH<sub>4</sub> the following relation has been derived from the PAI model for pure Argon [76]:

$$\sigma(I) / I = 0.41 \text{ (p d)}^{-0.32} \text{ N}^{-0.46} = 0.41 \text{ (pL)}^{-0.32} \text{ N}^{-0.14}, \tag{3.6}$$

where L is the total length over which I is measured. To allow comparison of different gases, an extension was proposed:

$$\sigma(I) / I = 0.345 \text{ (A p d)}^{-0.32} \text{ N}^{-0.46}$$
, with A = 6.83 v p D / (\beta^2 I), (3.7)

where v is the mean number of electrons per molecule. For He, Ne, Ar, Kr and Xe, A=0.32, 0.50, 0.62, 0.65 and 0.70 respectively. Values obtained from these theoretical relations based on a likelihood treatment were intended as a guide only to estimate best possible resolutions. Based on experimental results, it has been argued that below a sample size of about 5 cm atm in argon the gain in resolution is negligible [80]. More recent studies, however, indicate that sampling down to 0.5 cm atm still improves the accuracy [81].

Table 3 gives an overview of the PID performance of some TPCs. Included are also the Jet Chamber of OPAL at LEP and two big detectors, the EPI and ISIS2, which were dedicated to dE/dx measurements with only restricted tracking capability. The best measured values for  $\sigma(I)$  are compared with the ideal resolution obtained from the relations cited above, assuming the maximum number Nmax of samples can be used. The last row shows the calculated resolution for the case that only 70% of Nmax samples are useful, which is closer to reality in most cases. The measured values are very close to these theoretical numbers. For PEP4 and EPI, the best values are obtained for very clean tracks, where the assumption of Nmax contributing samples is reasonable.

**Table 3.** Best measured resolution values as compared to simulations [76], which assume Nmax or 0.7 Nmax as number of samples.

Param./	DED (	A A FEDAN	DEI DIN	GEL + D	00.11	EDY	YGYG 2
Experiment	PEP4	ALEPH	DELPHI	STAR	OPAL	EPI	ISIS2
Nmax	183	340	192	45	120	128	320
D [cm]	0.4	0.4	0.4	13x11.5	1.3	6	1.6
				32x19.5			
p [atm]	8.5	1	1	1	4	1	1
L [cm]	73	136	78	77	160	768	512
Best $\sigma(I)$ meas.	2.7	4.4	5.7	7.4	3.1	2.55	3.1
Ideal resol.,							
Nmax	2.5	3.8	4.9	6	2.7	2.5	2.5
N = 0.7  Nmax		4.4	5.8	7.1	3.1		2.9

#### 4. Particularities of some TPCs

#### 4.1. Global aspects

Many TPCs have been constructed. They may be grouped crudely according to the type of experiments they were or are part of.

### - (a) Electron / positron storage rings: PEP4, TOPAZ, ALEPH and DELPHI.

These experiments demanded large TPCs but had to handle only low rates of events with multiplicities of 2-30 charged tracks. Their designs are similar. PEP4 and TOPAZ were pressurized to maximize particle identification. ALEPH, the largest of these four TPCs, with the longest drift length (2.2 m) of all TPCs up to now and DELPHI put emphasis on momentum resolution, pattern recognition and reduced material in front of other components and chose operation at 1atm. The size of the DELPHI TPC had to be reduced because of the addition of a RICH for more powerful PID. Both ALEPH and DELPHI used circular pad rows to improve spatial resolution. ALEPH chose longer pads for better momentum resolution at the highest energies, DELPHI preferred shorter pads for better two track separation of lower momentum particles.

A reconstructed event from the PEP4 TPC is shown in figure 31.

### - (b) Heavy ions: fixed target and collider experiments.

Medium-sized and large TPCs have been used in a number of fixed target experiments: EOS/HISS at the BEVALEC, the BNL 810 TPC at Brookhaven and NA35, NA36 and NA49 at CERN. A very large TPC is operating for STAR at Brookhaven and an even larger one, ALICE, is ready for data taking at the LHC at CERN. All these TPCs have to handle high particle multiplicities up to several thousand per event in STAR and even more in ALICE. They use(d) cathode planes subdivided into a large number of pads, or densely spaced short sense wires (NA36, BNL810).

EOS was an early heavy ion experiment, using full pad coverage. It had a spatial resolution of 300  $\mu$ m and a two-track separation of 2.5 cm. The powerful mass separation by dE/dx is demonstrated in figure 32 [82].

NA 49 consisted of 4 large TPCs, two upstream inside a magnetic field, two outside, providing a long lever arm for momentum measurement. Simple thin field cages were used, in form of Al-coated Mylar strips stretched over posts, separated from the gas container. The maximum drift length was 1.1 m vertical, pads on the top. Figure 33 gives an indication of the PID in the relativistic-rise region by ionization sampling.

STAR, 4.2 m long and 4m in diameter, has operated in Au on Au collisions with 200GeV/nucleon at average luminosities up to 8x10<sup>27</sup> [84]. The unique pattern recognition of the TPC in multi-track events with more than 3000 tracks per central Au-Au event is visible in the display of a collision, figure 34. STAR was designed to separate pions from protons up to 1.2 Gev/c. Figure 35 shows the energy loss distribution for primary and secondary particles. On a statistical basis, PID has been achieved even in the relativistic rise region.

Starting first operation at the LHC, ALICE is the largest TPC constructed so far, with 5m diameter and 2.5 m drift length. To handle event multiplicities still higher than those of STAR, some 560 000 pads are read out, making use of highly integrated state-of-the-art electronics, see 3.2.7. Despite the high occupancy, PID is aimed for with a resolution of about 5% [77].

- (c) A group of TPCs with rather specific demands.

A few of them will be discussed below.

#### 4.2. Special aspects

#### **TRIUMF**

The experiment was designed specifically to search for the rare decay  $\mu Z \rightarrow e^{-}Z$  at the level of  $10^{-12}$  [85]. Particle identification was required over a large solid angle surrounding the target with good cosmic ray rejection, momentum resolution of about 1% and tolerance to high rates ( $10^6$  stopping muons/s). The novel TPC idea was picked up and with a simplified design and operation at 1 atm, the experiment could start around the same time as PEP4. The chamber had only 144 anode wires, each sitting in a rectangular cathode with a 6mm slot and above a pad row with  $6x19\text{mm}^2$  pads. The maximum drift length was 34 cm in 0.9 T.

#### CERES/ NA45

CERES [86] is a drift chamber with a radial, variable drift field, 2 m long and 2.6 m in diameter. It is located inside a very inhomogeneous magnetic field formed by two separated short coils. Calibration with laser beams is essential. It has about 15 000 pads of staggered chevron type. A resolution of 250-350  $\mu$ m in azimuth and 400-500  $\mu$ m radially was achieved.

#### MUNU TPC

The MUNU TPC [87], to study antineutrino-electron scattering near the Bugey reactor, kept the same structure as the Gotthard TPC (see below) but with a larger fiducial volume of  $10^3$  liters and was filled with  $CF_4$  at 3 atm. The power of continuous pattern recognition is again used to differentiate between electrons from Compton scattering, pair production and  $\beta\beta$ -decays. The TPC was contained in an acrylic vessel with fieldshaping rings, and immersed in a tank filled with liquid scintillator, viewed by photomultipliers. Spatial resolution was improved by better electronics but still limited by noise, as well as by granularity. Various R&D activities are pursued in view of the construction of a significantly larger TPC. One interesting result is that Micromegas detectors with a 225  $\mu$ m gap can achieve a gain above  $10^3$  in Ar/CF<sub>4</sub> (98/2) at 4 atm.

### МиСар

The muon capture experiment at the PSI has used a TPC 15 cm wide, 28 cm long and with a 12 cm drift height, filled with hydrogen at 10 atm and room temperature and operating at a gain of 60 [88]. The TPC allows offline definition of a clear fiducial volume 15 mm away from any material. For the next phase, a modified TPC has been commissioned to operate in  $D_2$  at 30° K and 4 atm and will read pad signals with a unit gain.

#### HARP

The HARP TPC [89], with 1.6 m drift length and 82 cm diameter and operated in Ar / CH<sub>4</sub> (91 / 9) has been used at CERN as a large-angle spectrometer, surrounding the target, for precision measurements of hadron production by protons and pions colliding with nuclei, making use of track reconstruction and PID. Corrections have been elaborated, which reduced serious track distortions due to inhomogeneities of the electric and magnetic fields and to beam variations to insignificant level and resulted in good physics performance.

### Liquid Argon 'TPC'

#### - ICARUS

A very large drift chamber filled with liquid Argon has been constructed and tested for the ICARUS project [90]. The T600 module contains 600 tons of Argon, is 18 m long and has a maximum drift length of 1.5 m. The xy-information is not obtained from pads but from 3 wire

planes 3mm apart, with wires (150  $\mu$ m  $\varnothing$  at 3 mm pitch) running at 0°, +60° and -60°, by induction when electrons are passing through the first two planes before they are collected on the last plane. The reconstruction of 3-D points is based on the fact that the drift time coordinate is shared amongst the three wire planes. The charge deposited by the particle is about 1.5 fC/mm. As the chamber works without amplification in the liquid, amplifiers with very low noise are required. The purity level of the LAr has to be extremely high, allowing only around 1 ppb of oxygen to keep electron attachment low. Excellent pattern recognition and energy resolution was achieved for cosmic ray events. An example [91] is shown in figure 36.

### - ArgoNeuT

The Argon Neutrino Teststand (ArgoNeuT) is installed at Fermilab in the NuMI neutrino beam upstream of MINOS [92]. Its purpose is to study interactions of low energy neutrinos (0.1-10 GeV) in a LAr TPC and gain valuable technical experience with construction and operation in view of building a similar detector on a much larger scale. Dimensions of the sensitive volume are 47x40x90 cm<sup>3</sup>. The readout structure is similar to that of ICARUS but with 4mm wire pitch and wire plane separation. The TPC started operation in 2009.

#### - MicrobooNe

MicrobooNe [93], an experiment at Fermilab, is to build and operate a LAr TPC with about 100 t. The experiment will measure low energy neutrino cross sections and investigate the low energy excess events observed previously, profiting from its good electron-gamma separation. The detector is considered as a necessary next step towards the construction of a kilo-ton range detector.

#### - ArDM

The goal is the operation of a bi-phase LAr detector of about 1 ton for Dark Matter search, 'with independent ionization and scintillation readout, to demonstrate the feasibility of a noble gas ton-scale experiment with the required performance to efficiently detect and sufficiently discriminate backgrounds for a successful WIMP detection' [94 a]. The readout is based on the LEM-TPC idea. Electrons drifting in the liquid argon are extracted at the liquid-vapour boundary into the vapour volume by the field of a double-grid, with one grid inside the liquid and the other in the vapour. From there they are attracted to and amplified in two Large Electron Multipliers (LEMs) and captured by an anode above. Signals are read from crossed strips on the anode and upper side of the second LEM. A LEM has a GEM-like structure (see section 5.2.2) but with larger dimensions:  $500 \, \mu \text{m}$  holes on a  $800 \, \mu \text{m}$  pitch in a 1.6 mm thick FR4 board. This design is supposed to facilitate large area construction.

A small prototype ( $10 \text{ cm}^2$  surface and 10 cm drift in the liquid) has been constructed to test the technique 94 (b)]. With cosmic muons, an effective gain of 10 has been achieved. This gain is considered sufficient to compensate the attenuation of charge collection for up to 10 m drift in LAr. On the other hand, gains > 100 are required to reach a low enough energy threshold for direct dark matter searches.

Another challenge for ArDM is to obtain an electron/ recoil rejection factor  $> 10^9$  (required because of the contamination of natural Ar with the isotope  $^{39}$ Ar, a beta-emitter with Q = 565 keV) by measuring very precisely the ratio of scintillation to ionization yields. Various light detection systems are being studied.

### - GLACIER

The Giant Liquid Argon Charge Imaging ExpeRiment (GLACIER) is a large underground observatory for proton decay search, neutrino astrophysics and CP-violation studies in the lepton sector [95]. The concept should be scalable up to a total mass of 100 kton. The proposed

cylindrical cryostat is based on industrial liquefied natural gas technology. Electrons have to be drifted over 20 m, requiring special care for achieving and maintaining high purity in the LAr and for the drift voltage of the order of a MV. The readout is based on the novel LEM technique (see above). Compared to the 'standard' wire readout, this technique is considered easier to scale to large size. In GLACIER there is also the possibility to detect Cherenkov light and 'conceiving to have a high T<sub>c</sub> superconducting solenoid in LAr'.

The project is supposed to proceed in steps, the first one being ArDM. The next step considered is a 10 t device, to test and optimize the readout methods and assess the calorimetric performance. Beyond these developments, 'a 1 kton-scale device is considered the appropriate choice for a full engineering prototype of a 100 kton detector.'

### Xe TPCs

The  $^{136}$ Xe isotope is a good source for studying neutrinoless double beta decay. The energy released is Q = 2.458MeV, higher than most of the radioactive decays from the U and Th chains. Nevertheless, excellent background suppression for energies near Q, is necessary to identify or exclude the neutrinoless events. The clear definition of the fiducial volume, combined with continuous tracking and good energy resolution of a TPC are crucial for this. Both gaseous and liquid fillings have been proposed. Gas offers in principle better energy resolution, electron tracking with identification of Bragg peak(s) and angular correlation and possibly easier identification of the final state ( $^{136}$ Ba $^+$ ). But the detector is less compact and scaling up is more difficult (pressure vessel).

The 'Gotthard TPC' [87] was filled with 180 liters of Xe gas at 5atm (5kg), enriched to 68% in <sup>136</sup>Xe with 5% CH<sub>4</sub> as quencher and used in the Gotthard tunnel. The readout was at the top with a standard grid and anode/potential wire plane. The cathode plane had perpendicular x and y strips with 4mm pitch. The anode signal was used to measure the total charge. A double beta decay candidate would show a single continuous track within the fiducial volume with enhanced energy deposition at both ends. In addition, an energy window around 2.46 MeV is defined with an energy resolution of 2.7% rms for the neutrinoless decay. No excess above background was found, which set a lower limit of the half-life of 4.4 x 10<sup>32</sup> years.

*NEXT* [96] is another proposal for a TPC using 100 kg of enriched gaseous Xe at 10bar, in a cylinder about 2 m long and 1 m in diameter. A first stage with 10 kg of natural Xe, Next-10, is foreseen to be built during the next 2-3 years.

Recently, an effort [97] has started to reach unprecedented energy resolution by not only measuring the ionization and scintillation light but by reducing the fluctuations from the amplification of the ionization signal, which destroy the benefit of the small Fano factor in Ar. Some amplification is required, as the fluctuation of the total charge from an absorption of 2,46 MeV is 120 electrons rms and electronic noise would dominate without gas amplification. The idea is to accelerate the electrons to an energy sufficient to excite optical states but not to ionize. The fluctuations from the electroluminescence should be small, as there is no avalanche process involved: photons do not excite additional emissions. A test setup is being assembled at LBNL to demonstrate electroluminescent internal gain in a high pressure gas. Photomultipliers record primary scintillation and provide a start for the drift time, SiPMs perform tracking.

A liquid Xe TPC, EXO-200, is presently being commissioned at WIPP [98]. It uses 200kg of enriched liquid Xe and detects both scintillation and ionization. It is meant as a prototype for a ton-scale detector. Exo-200 is a cylinder, 35cm long and 40cm in diameter. It has a central cathode and both ends are equipped with induction and charge collection crossed wire grids followed by large avalanche photodiodes (1.6 cm active diameter). The simultaneous readout of scintillation and ionizations improves the energy resolution.

A LXe TPC has also been proposed for a small PET system (inner diameter 14 cm, outer 38 cm, length 8 cm), making use of the high light yield and short decay time (98% in 2.2 ns) in Xe and the good spatial and energy resolution of a TPC [99]. A small test chamber gave a combined energy resolution of 3.9% rms from light measured with APDs and from ionization of 511 keV electrons. First tests of a sector prototype  $(2\pi/12)$  started in 2008. Two sidewalls carry APDs and the readout is from anode wires and cathode strips.

#### Radial TPCs

#### STAR Forward TPCs

Two cylindrical forward TPCs have been added to the STAR experiment to increase the coverage at small angles to the beam [100]. A radial drift field (perpendicular to the solenoid field) was chosen to improve 2-track separation close to the beampipe to 1-2 mm. Each 1.2 m long TPC is split into 5 planar slices with an inner tube on HV (R = 7 cm) and an outer wall at ground potential (R = 30 cm) and containing the readout chambers. The chambers follow the curvature and cover  $2\pi/6$ . They contain two rings of pad rows with pads 1.9 mm in  $\varphi$  and 20 mm along the beam. The anode wires are at 1.5 mm from the pads and cross these at 17.4° to avoid a steplike structure of the response around  $\varphi$ . An Ar/CO<sub>2</sub> (50/50) mixture was chosen for low diffusion and small Lorentz angle. Because of the slow drift, a pulse shaping time of 350 ns was retained and 5 MHz sampling.

#### **BONUS**

A small TPC (12cm diameter, 20cm length) has recently been operated at Jefferson Lab in studies of neutron structure from electron-neutron interactions [101]. It allows identification and measurement of spectator protons. The radial field was preferred for better acceptance of low-momentum protons. It is the first experiment using a curved Triple-GEMs for gas amplification. A He/DME (4/10) mixture was chosen to minimize energy loss by the protons and to provide stable operation with sufficient gain.

### **Spherical TPC**

The idea of a spherical TPC is being investigated around various applications demanding detection of low energy neutrinos. The *NOSTOS* project [102], for the observation of neutrino oscillations, foresees a TPC with an inner sphere of 1m diameter and an outer sphere of 20m diameter. The inner sphere should contain some 20 kg of tritium and be covered with Micromegas detectors (see 5.2.1). The inter-sphere drift volume is to be filled with Xe at 10atm. The spherical geometry has the advantage of minimizing the detector surface, being a source for background, for a given volume. A prototype spherical drift chamber only sampling radial information (i.e. not providing 3-D points) is being tested. The outer vessel has 1.3m diameter. In the centre is mounted a 1cm diameter sphere acting as single readout channel. With  $Ar/CO_2$  (90/10) and Ar/Isobutane (98/2) a gas amplification above  $10^4$  has been achieved.

This structure has recently been used with an inner sphere of 1.6 cm diameter as a proportional counter. It has shown good energy resolution [102 b] and has been used to measure thermal neutrons with a <sup>3</sup>He filling [102 c]. A risetime cut permitted good background rejection.

### 5. Gas amplification without anode wires

To date, gaseous TPCs of almost all experiments had MWPCs as readout chambers, One exception is the T2K experiment, which started taking data with TPCs using Micromegas readout. Out of a number of readout techniques avoiding anode wires, which have been proposed for TPCs, we shall discuss three options: Parallel Plate Chamber (two versions), Micromegas and GEM structures. The first one is a relatively old idea, the latter two have raised interest mainly in connection with TPC projects for a future 0.5-3TeV Linear Collider (LC). The goal is improved spatial resolution by suppressing the ExB contribution and finer granularity for two-track separation. The present design specifications for a TPC at the *Linear Collider* are:

Number of points/track up to 200-250

 $\begin{array}{ll} Point \ resolution, \ rms & 100\text{-}140 \ \mu\text{m} \ (r\phi) \ ; \ \sim \! 1\text{mm} \ (z) \\ Double-track \ separation & 2\text{-}3 \ mm \ (r\phi) \ ; \ \sim \! 1\text{cm} \ (z) \\ Momentum \ resolution \ (TPC) & \sigma \ / \ p_t^2 \sim \! 2 \ x \ 10^{\text{-}4} \ GeV^{\text{-}1} \end{array}$ 

dE/dx resolution, rms 4-5%

Minimum material  $4\% X_0$  centrally,  $15\% X_0$  forward

Thus, the demands for the LC go beyond the performance of existing designs with respect to spatial resolution, two-track separation and material thickness.

#### 5.1. Parallel Plate Chamber

Parallel Plate Chamber technology has since long found many applications, in the discharge mode as fast counters and spark chambers and in a 'sub-discharge' mode in streamer chambers. During the final development phase for the LEP TPCs. two proposals were made simultaneously for a use in the proportional mode.

The first proposal [103], called Parallel Plate Avalanche Chamber (PPAC), grew out of the development of multi-gap avalanche chambers and is sketched in figure 37. One coordinate is read out in the HV3 plane from 100  $\mu$ m wires with a 500  $\mu$ m pitch, the other one from orthogonal wires or pads in the HV4 plane. Tests were done with wires read-out, with and without additional amplification between HV3 and HV4. HV2 is a wire mesh.

The other proposal, called Pad TPC [104], grew out of the idea to avoid amplifying wires altogether and to have a natural geometry for implementing circular pad rows, see figure 38. The pads are the anode, the HV being applied to the mesh cathode, which terminates the drift volume. Circular pad rows had at that time not yet been implemented in the standard TPCs with amplifying anode wires. It was thought that complicated corrections would be required due to the variable angle between wire and pad row directions. This finally turned out not to be a problem and circular pad rows were introduced by ALEPH and DELPHI. In the proposal for a Pad TPC, resistive charge division had also been suggested, with discrete components or with a resistive layer, to increase the readout pitch (lowering the channel count and cost) but keeping the good spatial resolution [105].

Despite the fact that none of the proposals was followed up because MWPCs were considered more advanced and thus a safer choice, it is useful to look at the advantages claimed, because these re-appear in the new options presently under study.

Gains up to  $10^5$  were achieved with Ar/CH<sub>4</sub> mixtures and amplification gaps of 3 and 4mm. A gain G of  $3x\ 10^4$  requires an amplification field  $E_A = 13.75\ kV$  / cm with a 4 mm gap in Ar/CH<sub>4</sub> (80/10). As  $G = e^{\alpha d}$ , where  $\alpha$  is the first Townsend coefficient and d the gap width, one deduces  $\alpha = 25.8$  / cm.

#### - Positive ion feedback

As the ion feedback ratio into the drift volume depends on the ratio of the drift field divided by the amplification field it is around 1 % in the parallel plate amplification scheme compared to 10-20% in the standard MWPC.

### - Two-track separation

The avalanche has a width of only 1 mm FWHM, as measured in the PPAC. A two-track separation in  $r\phi$  down to 2 mm should in principle be achievable. This is much better than with the standard TPC. A read-out with closely spaced, thin pads, however, would be required to make use of this potential, possibly with resistive charge division.

The two-track separation in the drift direction can in principle also be of the order of 2mm with fast pulse shaping. The fast electron movement induces about one tenth of the total charge in  $\leq 10$ ns, as most of the charge is produced at a distance of about  $(1/\alpha)$  cm. The ions move so slowly that they contribute very little: with integration over 100ns the total induced charge would be increased only by 10 to 12.5% from the contribution of  $CH_4$ -ion drift. Using the electron signal means of course an effective gain of  $G_{eff} = e^{\alpha d} / \alpha d$  only, i.e. in our example about one tenth of the gas amplification. Pads in a standard TPC with field wires see an effective gain of < 20% of the avalanche charge at 1 atm and less at higher pressure.

### - Space point resolution

Due to the large suppression of the  $\mathbf{E}$  x  $\mathbf{B}$  effect in the PPAC (with narrow pitch of the anode wires) and almost complete suppression in the Pad TPC, a significant improvement on the spatial resolution in  $r\phi$  is expected and the suppression of the asymmetry between positive and negative curvature.

### 5.2. Micromegas

A schematic view of the Micromegas (MICRO-MEsh GASeous structure) [106] and the electric field lines is shown in figure 39. The electrons from the track ionization pass through a fine mesh into the amplification gap and are multiplied in the high field, inducing signals on the anode plane segmented into read-out pads. The 'micromesh' is woven from 16  $\mu$ m wires, leaving holes of about (50 $\mu$ m<sup>2</sup>). In contrast to the Pad TPC, the Micromegas has a gap of only (50 - 100)  $\mu$ m. Small pillars support the mesh every 2.5 mm to guarantee adequate flatness.

Chambers have been in use in some experiments, e.g. in Compass, where 12 chambers (40x40) cm<sup>2</sup> obtained resolutions of 70-90  $\mu$ m and 9 ns and operated in particle fluxes up to 25 MHz / mm<sup>2</sup>.

To obtain sufficient amplification in the thin gap, a very high electric field of 30-80 kV/cm is required. As a consequence of the high amplification-field/ drift-field ratio, the electrons enter through a very narrow funnel. Electron diffusion increases in the high field and causes the avalanche to spread beyond the original funnel to a width of about 35  $\mu$ m FWHM. This in turn is reducing the positive ion feed-back to about 0.2%, as ions produced outside the original funnel will be trapped by the grid. No change of ion feed-back was observed for B = (0-2) T.

The signal formation in a Micromegas is very fast, also the component due to the positive ions, as these reach the mesh in less than 50-100 ns. As a result, even with fast signal shaping most of the total avalanche charge  $N_0 e^{\alpha d}$  is seen and not only the electron component  $N_0 e^{\alpha d} / \alpha d$ .

For pad widths  $\geq$  (1-2) mm, the avalanche is too narrow and the 'pad response width' has to be broadened to enable charge interpolation. This broadening has been achieved by laminating to the anode a Mylar film coated with a high surface resistivity material (e.g. CERMET-Al-Si alloy with 1 MΩ/square). With pads of 2x6 mm and a gap of 50  $\mu$ m, a resolution of 50  $\mu$ m was measured with gas gains of 2300 and 4700, not depending on drift length for up to 15 cm drift in 5T. A gas mixture of Ar/CF<sub>4</sub>/iso-butane (95/3/2), the so-called T2K gas, was chosen for its high electron drift velocity (7.3 cm/ $\mu$ s) at E = 200V/cm and for the high  $\omega\tau$  at 5 T, reducing the single electron transverse diffusion to 190  $\mu$ m / 1m drift [107]. From the measured resolution it was estimated that some 27 electrons (= N<sub>eff</sub>) were statistically relevant for the centroid determination. This is close to the most probable ionization for 6 mm long pads.

Also the Micromegas has some ExB effect in the holes of the grid but this is insignificant because of the small dimensions.

Various systems are being studied, in which the printed circuit board anode with pads is replaced by Si-pixel devices ('Digital TPC'), with and without enlarged metallic pixels, with a separate Micromegas mesh or an integrated grid and with resistive protection layers of aSi:H or  $Si_3N_4$  [108]. The digital pixel readout does not require signal broadening.

The first large experiment using Micromegas as read-out chamber for a TPC is T2K [109]. It employs what is called 'bulk-Micromegas', in which the whole structure combining the multilayer read-out plane, the mesh and the pillars produced by photolithographic etching procedures as a unit, in form of (40x40) cm² plates [110]. The gap is 128  $\mu$ m and the 0.3 mm pillars have a pitch of 2.5 mm, providing about 93% active surface. The pads are about (7x10) mm², read out via blind holes and screened lines on the back. A gain variation of 2.2% was achieved after corrections for capacitance. Operating in 0.2 T, the TPCs are to provide a 10% momentum resolution at 1 GeV/c and separation of electrons from muons by dE/dx.

MIMAC [111] is a multi-chamber detector for Dark Matter search. It is planned to do tracking and measure ionization with a matrix of TPCs filled with  $^3$ He and CF $_4$  (gases with sensitivity to spin-dependent interactions), with Micromegas as detector with high granularity readout. As a first step, a small prototype has provided the first measurement of He ionization in He down to recoil energies of 1 keV, important for the use of He in dark matter search. In a second step, 3-D reconstruction of tracks of 5 MeV  $\alpha$ -particles has been achieved in He/Isobutane (95/5) at 800 mbar. For this measurement the anode had x and y strips at a 200  $\mu$ m pitch. The tests are being extended to recoil energies below 6 keV, the range of interest in Dark Matter search.

### **5.3.** Gas Electron Multiplier (GEM)

The Gas Electron Multiplier (GEM) [112] is produced by chemically etching holes at high density into a thin metal-coated polymer foil. Gas amplification is achieved inside the holes by applying a voltage on the metal layers. Figure 40 shows the layout of the holes, electric field lines and a 'triple-GEM' structure with an anode plane for readout [113]. Typical parameters are: Foil thickness =  $50 \, \mu \text{m}$ , hole pitch =  $140 \, \mu \text{m}$ , inner hole diameter =  $70 \, \mu \text{m}$ , voltage = around  $400 \, \text{V}$ .

Three GEMs are usually put in series, to obtain sufficient gain with acceptable discharge probability. From the last GEM foil, the electrons drift through the induction gap to the anode segmented into pads or strips. For homogeneity reasons, the minimum gap width is about 1mm. The induced pulse has an intrinsic spread of about 350  $\mu$ m rms. The signal contains basically only a fast electron component, as there are no ions produced in the last induction gap except very near the holes of the last GEM foil.

A system of 20 triple-GEMs with an active area of (31x31) cm<sup>2</sup> were operated in COMPASS [114], in a high intensity muon beam. A spatial resolution of 70  $\mu$ m was achieved at rates up to 2.5 MHz / cm<sup>2</sup>. With 50ns pulse shaping and an effective gain of 8000, the efficiency was 99%. The much shorter peaking time of 10 ns applied in LHCb [115] led to a lower efficiency of  $\geq$  96% for two triple-GEMs in OR. The gain was 6000 in Ar/CO<sub>2</sub>/CF<sub>4</sub> (45/15/40).

Several experiments have observed charge build-up on the insulator inside the holes, which changes with particle flux and causes gain changes, reproduced by simulation [116].

For the TPC development, various read-out schemes are being studied, similar to those with Micromegas: standard printed circuit boards with pads, as well as Si pixels. High resolution (40  $\mu$ m for short drift) and granularity was demonstrated with a combination of a triple-GEM and Medipix/Timepix readout with (55x55)  $\mu$ m<sup>2</sup> pixels [117].

Ion feed-back is intrinsically low in a triple-GEM and further reduced in a magnetic field, to 0.25% at B = 5 T with alternating low and high drift/transfer fields [118 (a)]. Similar values are achieved with equal transfer fields but very low drift field (< 100 V / cm atm) in the TPC [118 (b)].

The LC-TPC collaboration has constructed a TPC prototype, 60 cm long and 70 cm in diameter, to study many aspects of a TPC for the Linear Collider, including various Micromegas and GEM read-out structures [119]. Some of the developments mentioned are certainly very encouraging but most are still far from use on a large scale.

## 6. Conclusions

Designed some 30 years ago to provide complete event information at low event rates around 1Hz and with particle multiplicities around 20 particles per event, TPCs have developed into unique devices to study heavy ion collisions with extreme multiplicities of up to several thousand particles per event and registering some hundred events per second. There is no competitor in this field delivering similar event details on a large scale. Besides this, TPCs have found applications in other fields, in particular for the detection of rare reactions/decays. As may be judged from the ongoing projects, it is unlikely that interest will be fading in the near future, because of the unique capability of the TPC to provide practically continuous 3-D spatial and ionization information of high granularity.

## References

- [1] G. Charpak et al., The Use of Multiwire Proportional Counters to select and localize Charged Particles, Nucl. Instr. and Meth. 62 (1968) 262.
- [2] T. Bressani, G. Charpak, D. Rahm and C. Zupancic, Track Localization by Means of a Drift Chamber, Proc. of the Int. Seminar on Filmless Spark and Streamer Chambers, Dubna, USSR, (1969) 275.
- [3] A.H. Walenta, J. Heintze and B. Schürlein, The Multiwire Drift Chamber A Novel Type of Proportional Wire Chamber, Nucl. Instr. and Meth. 92 (1971) 373
- [4] (a) D. Nygren, PEP-198-1975;
  - (b) "Proposal for a PEP Facility based on the TPC", PEP4 Dec30, 1976,
- [5] T. Lohse and W. Witzeling, The TPC, in 'The advanced Series on Directions in High Energy Physics', vol. 9, (1992), 82; ed. F. Sauli, World Scientific, Singapore.
- [6] (a) CERN Courier Jan/Feb 2004,
  - (b) V. Lepeltier, J.Phys., Conf. Ser. 65 (2007) 012001
  - (c) D. Attié, Nucl. Instr. and Meth. A598 (2009) 89-93

- [7] W. Blum, W. Riegler and L. Rolandi, Particle Detection with Drift Chambers, 2. ed., Springer-Verlag (2008).
- [8] H. Spieler, Semiconductor detector systems, Oxford Univ. Press, 2005.
- [9] I. Smirnov, Heed: Interactions of particles with gases,

http://consult.cern.ch/writeup/heed/

[10] R. Veenhof, Garfield – Simulation of gaseous detectors,

http://consult.cern.ch/writeup/garfield/

[11] S. Biagi, Magboltz: Transport of electrons in gas mixtures,

http://consult.cern.ch/writeup/magboltz/

- [12] H. Bichsel, (a) Nucl. Instr. and Methods A 562 (2006) 154;
  - (b) Phys. Letters B 667 2008) 267.
- [13] F. Lapique and F. Piuz, Nucl. Instr. and Meth. 175 (1980) 297-318
- [14] H. Fischle, J. Heintze and B. Schmidt, Nucl. Instr. and Methods 301 (1991) 297.
- [15] Review of Particle Physics, Phys. Letters B, 667, (2008): p.292, F. Sauli and P. Titov; p. 298, D. Karlen.
- [16] ICRU Report 31(1979), 'Average energy required to produce an ion pair', Washington D.C.
- [17] I. Lehraus et al. Nucl. Instr. and Meth. 153 (1978) 343.
- [18] W.W.M. Allison et al. Nucl. Instr. and Meth. 224 (1984) 396.
- [19] A.H. Walenta et al., Nucl. Instr. and Meth. 161 (1979) 45.
- [20] W. Blum et al., Nucl. Instr. and Meth. A 252 (1986) 407-412.
- [21] (a) M. Kobayashi, Nucl. Instr. and Meth. A 562 (2006) 136-140.
  - (b) D.C. Arogancia et al., Nucl. Instr. and Meth. 602 (2009) 403-414.
- [22] (a) L.C. Pitchford and A.V. Phelps, Phys. Rev. A, 25, 1 (1982) 540
  - (b) R.E. Robson and K.F. Ness, Phys. Rev. A, 33, 3 (1986) 2068
  - (c) K.F. Ness, Aust. J. Phys.48 (1995) 557.
- [23] S.F. Biagi, Nucl. Instr. and Meth. A283 (1989) 716.
- [24] B. Schmidt, Doctoral thesis, Univ. Heidelberg (1986).
- [25] (a) G. Schultz, Doctoral thesis, Univ. Louis-Pasteur, Strasbourg, (1979);
  - (b) G. Schultz, G. Charpak and F. Sauli, Revue de Ph. Appl. 12 (1977) 67.
- [26] F. Sauli, CERN 77 09 (1977).
- [27] E.W. McDaniel and E.A. Mason, The Mobility and Diffusion of ions in gases, Wiley, New York 1973.
- [28] J.H. Hornbeck, Phys.Rev.84 (1951) 615, <a href="http://link.aps.org/abstract/PR/v84/p615">http://link.aps.org/abstract/PR/v84/p615</a>; copyright (2010) APS for figure 3.
- [29] E.B. Wagner, F.J. Davies and F.J. Hurst, J. Chem. Phys. 47 (1967) 3138.
- [30] B. Schmidt, Diploma thesis, Univ. Heidelberg (1980).
- [31] RD-32, CERN/DRDC 94-10 (1994)
- [32] S.R. Amendolia et al., Nucl. Instr. and Methods 244 (1986) 516.
- [33] A. Ishikawa, (a) <a href="http://www-hep.phys.saga-u.ac.jp/ILC-TPC/gas/">http://www-hep.phys.saga-u.ac.jp/ILC-TPC/gas/</a>
  - (b) <a href="http://www-hep.phys.saga-u.ac.jp/ILC-TPC/gas/ps/">http://www-hep.phys.saga-u.ac.jp/ILC-TPC/gas/ps/</a>
- [34] H.S.W. Massey, E.H.S. Burhop and H.B. Gilbody, Electronic and ionic impact Phenomena, Clarendon, Oxford (1969).
- [35] D.L. McCorkle, L.G. Christophorou and S.R. Hunter, Proc. 2<sup>nd</sup> Int. Swarm seminar, Oak Ridge, USA, Pergamon, New York (1981) 21.
- [36] F. Bloch and N.E. Bradbury, Phys. Rev. 48 (1935) 689.
- [37] G.A. Erskine, Nucl. Instr. and Meth. 105 (1972) 565.
- [38] S. Ramo, Proc. I.R.E.27(1939) 584.
- [39] W. Shockley, J. Appl. Phys. 9 (1938) 635.
- [40] Collected by A. von Engel, Handbuch der Physik 21 (1956), Springer, Berlin.
- [41] (a) S.F. Biagi, Nucl. Instr. and Meth. A283 (1989) 716;
  - (b) J.C. Armitage, Nucl. Instr. and Meth. A271 (1988) 588.

- [42] M.E. Rose and S.A. Korff, Phys. Rev. 59 (1941) 850.
- [43] W. Diethorn, USAEC Report NY6628 (1956).
- [44] G.D. Alkahazov, Nucl. Instr. and Meth. 89 (1970) 155.
- [45] S.C. Curran, A.L. Cockroft and J. Angus, Phil. MAG. 40(1949) 929.
- [46] W. Legler, Z. Naturforschung 16a (1961) 253.
- [47] H. Schlumbohm, Z. Phys. 151 (1958) 563.
- [48] C. Brand et al. Nucl. Instr. and Meth. A 237 (1985) 501.
- [49] M.Anderhub, M.J.Devereux and P.G.Seiler, Nucl. Instr. and Meth. 166 (1979) 581-2.
- [50] J.Bourotte and B. Sadoulet, Nucl. Instr. and Meth. 173 (1980) 463.
- [51] H.J.Hilke, Nucl. Instr. and Meth. 174 (1980) 145.
- [52] M. Towrie et al., J. Phys.B 19 (1986) 1989.
- [53] S.L.T. Dysdale et al., Nucl. Instr. and Meth. A252 (1986) 521.
- [54] G.Hubricht et al., Nucl. Instr. and Meth. 228 (1985) 327; 243 (1986) 495.
- [55] H.J.Hilke, Nucl. Instr. and Meth. A 252 (1986) 169; ref. herein can be updated:
  - [21] Instr. Exp. Tech. USSR 27 (1984) 546; [22]: Instr.Exp.Tech.USSR 28 (1985)1
  - [25] Nucl. Instr. and Meth. A243 (1986) 495.
- [56]E.M. Gushchin, A.N. Lebedev and S.V.Somov, Instr.Exp.Tech.USSR28 (1985) 1.
- [57] J. Abele, Nucl. Instr. and Meth. A 499 (2003) 692.
- [58] A. Lebedev, Nucl. Instr. and Meth. A 478 (2002) 163.
- [59] a) J. Va'vra, Nucl. Instr. and Meth. A 252 (1986) 547,
  - b) J. Va'vra, Nucl. Instr. and Meth. A 515 (2003) 1,
  - c) J. Kadyk, Nucl. Instr. and Meth. A 300 (1991) 436,
  - d) N. Tesch, IEEE Transactions on Nucl.Sc. 49 (2002) 1609.
  - e) M. Capeans, Nucl. Instr. and Meth. A 515 (2003) 73.
  - f) R. Bouclier et al. Nucl. Instr. and Meth. A 350 (1994) 464.
- [60] a) Proc. of the Workshop on Radiation damage to Wire Chambers, Berkeley (org. J. Kadyk), LBL 21170 (1986).
  - b) Proc. of the Int. Workshop on Aging Phenomena in Gaseous Detectors, Hamburg, 2001, Nucl. Instr. and Meth. A 515 (2003), 1-386.
  - c) NASA, A very large database on outgassing of materials can be reached via the NASA homepage.
- [61] J. Adam et al., Nucl. Instr. and Meth. 217 (1983) 291.
- [62] L. Malter, Phys. Rev. 50 (1936), 48.
- [63] ATLAS Collaboration, The ATLAS Experiment at the CERN LHC, J. of Instr., JINST 3 S08002 (2008).
- [64] G.R. Lynch, Performance of the PEP4 TPC, Seminar at MPI-Munich, June 22, 1987; and private communication 1991.
- [66] R. Veenhof, http://rjd.web.cern.ch/rjd/Harp/charge.html
- [67] S.R. Amendolia et al. Nucl. Instr. and Meth. A 234 (1985) 47.
- [68] P. Nemethy et al., Nucl. Instr. and Meth. A 212 (1983) 273.
- [69] (a) R. C. Jared, D.A. Landis and F.S. Goulding, IEEE Trans. Nucl. Sc., NS-29, 1, (!982) 57(b) H. Aihara et al. IEEE Trans. Nucl. Sc., NS-30, 1, (!983) 162
- [70] (a) R. Campagnolo, HEP 2005, Int. Europhysics Conf., EPS, Lisboa
  - (b) B. Mota et al. NIM A 535 (2004) 500
- [71] R. Veenhof, <a href="http://rjd.web.cern.ch/rjd/Harp/signal.html">http://rjd.web.cern.ch/rjd/Harp/signal.html</a>
- [72] (a) D. Decamp et al., Nucl. Instr. and Meth. A 294 (1990) 121.
  - (b) W.B. Atwood et al., Nucl. Instr. Meth. A306 (1991) 446
- [73] (a) P. Aarnio et al., Nucl. Instr. Meth. A 303 (1991) 233
  - (b) Y. Sacquin, Nucl. Instr. Meth. A 323 (1992) 209
  - (c) P. Abreu et al., Nucl. Instr. Meth. A 378 (1996) 57
- [74] W. Blum et al., Nucl. Instr. and Meth. A 252 (1986) 407.

- [75] A. Alikhanov et al., Proc. CERN Symp. On High Energy Accel. Pion Phys. 2 (1956) 87, CERN, Geneva.
- [76] W.W.M.Allison and J.H. Cobb, Ann. Rev. Nucl. Part. Sci. 30 (1980) 253.
- [77] P.Christiansen and J. Baechler, ALICE-INT-2005-030 (2006).
- [78] H. Bichsel, Nucl. Instr. and Meth. A562 (2006) 154.
- [79] I. Lehraus, R. Matthewson and W. Tejessy, Nucl. Instr. and Meth. 200 (1982) 199.
- [80] (a) A.H. Walenta et al., Nucl. Instr. and Meth. 161 (1979) 45;(b) I. Lehraus et al., Nucl. Instr. and Meth. 196 (1982) 361.
- [81] R. Assmann, Diploma thesis, Univ. Munich, 1990.
- [82] M. Ronan, Second 'rare event' TPC workshop, Paris, Dec 2004
- [83] D. Varga for NA49 Experiment, IEEE Nucl. Sc. Symp. 2008, Dresden
- [84] (a) M. Anderson et al., Nucl. Instr. and Meth. A 499 (2003) 659-678
  - (b) http://www.star.bnl.gov/STAR/magelib/collisions2001/ev\_2front.jpg
- [85] (a) C K Hargrove et al., Nucl. Instr. and Meth. 219(1984) 461-471,(b) H.Mes et al., Nucl. Instr. and Meth. 225 (1985) 547-549
- [86] D Adamova et al. Nucl. Instr. and Meth. A593 (2008) 203
- [87] J.L. Vuilleumier, J.Phys. Conf.Series 179 (2009) 012013
- [88] P. Kammel for the MuCap Collab., Few Body Systems (2008) 44: 333-336; DOI 10.1007/s00601-008-0321-8
- [89] V. Ammosov et al., Nucl. Instr. and Meth. A 588 (2008) 294-317
- [90] C. Rubbia, The Liquid Argon Time Projection Chamber: A New Concept for Neutrino Detectors, EP Internal Report 77-8, CERN (1977).
- [91] (a) ICARUS Collaboration, Nucl. Instr. and Meth. A 527 (2004) 329.
  - (b) E. Calligarich, ICARUS, Time Projection Chamber Symp., LBNL, Berkeley 2003
- [92] http://t962.fnal.gov/
- [93] http://www-microboone.fnal.gov/
- [94] (a) http://neutrino.ethz.ch/ArDM/
  - (b) A. Badertscher et al. Nucl. Instr. and Meth. A 617 (2009) 188-92,
  - (c) A. Bondar et al., Nucl. Instr. and Meth. A(2008), Eprint arXiv:0807.0530
- [95] A. Badertscher et al., arXiv:1001.0076v1[physics.ins-det] Dec. 2009
- [96] NEXT: J. Diaz et al., J.Phys. Conf. Series 179 (2009) 012005
- [97] D. Nygren, (a) TPC Symposium, LBNL, Berkeley, Oct.2003;
  - (b)D. Nygren, Nucl. Instr. and Meth. A 603 (2007) 337,
  - (c) H. Spieler et al., VCI (2010), to be publ. in Nucl. Instr. and Meth..
- [98] R. Gornea, for EXO Collab., J. Phys., Conf. Series 179 (2009) 012004
- [99] P. Amaudruz et al., IEEE Nucl. Sc. and Med. Imag. Conf. 2008, Dresden, Germany.
- [100] K H Ackermann et al., Nucl. Instr. and Meth. A 499 (2003) 713-719.
- [101] H Fenker et al., Nucl. Instr. and Meth. A 592 (2008) 273-286
- [102] P. Gorodetzky et al., Nucl. Phys. B 151 (2006) 410
  - (b) as proportional counter only: Y.Giomataris et al., JINST 3 P09007, 2008.
  - (c) S. Andriamonje et al., J. Phys, Conf. Series 179 (2009) 012003
- [103] A. Peisert, Nucl. Instr. and Meth. 217 (1983) 229.
- [104] H.J. Hilke, Nucl. Instr. and Meth. 217 (1983) 189.
- [105] based on suggestions by V. Radeka; (a) V. Radeka and R.A. Boie, NIM 178(1980) 543;(b) B.Yu et al., NIM A323 (1992) 413.
- [106] (a) Y. Giomataris et al., Nucl. Instr. and Meth. A 376 (1996) 29;
  - (b) Y. Giomataris, Nucl. Instr. and Meth. A 419 (1998) 239.
- [107] M. Dixit et al., Nucl. Instr. and Meth. A581 (2007) 254.
- [108] J. Timmermans, CLIC09 workshop, CERN, Geneva..
- [109] C. Giganti, 4<sup>th</sup> Symp. On large TPCs for low energy rare event detection, J.Phys., Conf. Ser. 179 (2009) 012002, Paris, France.

- [110] Y. Giomataris et al., Nucl. Instr. and Meth. A560 (2006) 405; R. de Oliveira, private communication 2009.
- [111] http://lpsc.in2p3.fr/mimac
- [112] F. Sauli, Nucl. Instr. and Meth. A 386 (1997) 531.
- [113] M. Hoch, Nucl. Instr. and Meth. A 535 (2004) 1
- [114] B. Ketzer et al., Nucl. Instr. and Meth. A 535 (2004) 314.
- [115] LHCb Collaboration, The LHCb Detector at the LHC, J. of Instr., JINST 3 S08004, (2008)
- [116] V.Tikhonov and R. Veenhof, Nucl. Instr. and Meth. A 478 (2002) 452.
- [117] A. Bamberger et al. Nucl. Instr. and Meth. A 581 (2007) 274.
- [118] (a) M. Killenberg et al., Nucl. Instr. and Meth. A 530 (2004) 251-257,
  - (b) A. Breskin et al., Nucl. Instr. and Meth. A 478 (2002) 225-229.
- [119] K. Dehmelt, TIPP09 (2009), KEK, Tsukuba, Japan.
- [120] IAEA-TECDOC-799 (1995), 'Atomic and Molecular Data for Radiotherapy and Radiation Research', IAEA Nuclear Data Section, Vienna, Austria.
- [121] E. Gatti et al., Nucl. Instr. and Meth. 163 (1979) 83-92
- [122] R. Bellazzini et al., IEEE Trans. Nucl. Sc. NS-32,1 (1985) 389-392
- [123] D. Fanscher and A.C. Schaffer, IEEE Trans. Nucl. Sc. NS-26 (1979) 150

For convenience, references for some TPCs have been grouped together below under the name of the experiment.

- [ PEP 4 ]: (a) D.R. Nygren, Proposal to investigate a novel concept in particle detection, LBL internal report, Berkeley, February 1974;
  - (b) Proposal for a PEP Facility based on the Time Projection Chamber, PEP4, Dec 1976;
  - (c) D. Fancher et al. Nucl. Instr. Meth. 161 (1979) 383-390;
  - (d) H. Aihara et al. IEEE Trans. Nucl. Sc. NS-30, 1,(1983) 63, 76 and 162;
  - (e) G.D. Cowan, PhD thesis, LBL-24715 (1988);
  - (f) G. Lynch, Seminar at MPI-Munich, June 22, 1987.
  - (g) R. C. Jared, D.A. Landis and F.S. Goulding, IEEE Trans. Nucl. Sc., NS-29, 1, (1982) 57
- [ TRIUMF ]: (a) C. K. Hargrove et al. Nucl. Instr. Meth. 219 (1984) 461;
  - (b) gating: H. Mes et al. NIM 225 (1984) 547;
  - (c) gating: D.A. Bryman Nucl. Instr. Meth. A 234 (1985) 42
- [ TOPAZ ]: (a) A. Shirahashi et al., IEEE Trans. Nucl. Sc. NS-35, 1 (1988) 414;
  - (b) T. Kamae et al., Nucl. Instr. Meth. A252 (1989) 423
- [ ALEPH ]: (a) W.B. Atwood et al., Nucl. Instr. Meth. A306 (1991) 446;
  - (b) D. Decamp et al., NIM A294 (1990) 121;
  - (c) gating: S.R. Amendolia et al., NIM A252 (1986) 403
- [ DELPHI ]: (a) P. Aarnio et al., Nucl. Instr. Meth. A303 (1991) 233
  - (b) Y. Sacquin, Nucl. Instr. Meth. A323 (1992) 209
  - (c) P. Abreu et al., Nucl. Instr. Meth. A378 (1996) 57;
- [ NA35 ]: (a) The NA35 Collaboration, CERN-SPSC-89-17 and SPSC/M-440 (1989);
  - (b) P. Jacobs for the NA35 and NA49 Collaboration, LBL-33810 (1993), Berkeley;
  - (c) M. Gazdzicki for the NA35 Collaboration, Nucl. Phys. A590 (1995) 197
- [ EOS/ HISS ] : G.Rai, IEEE Trans. Nucl. Sc., 37 (1990) 56
- [ NA 49]: (a) S. Afanasiev et al., Nucl. Instr. Meth. A430 (1999) 210;
  - (b) C. Alt et al., Eur. Phys. J. C 45 (2006) 343
- [ CERES/ NA45 ]: D. Adamova, Nucl. Instr. Meth. A593 (2008) 203
- [ STAR ]: M. Anderson et al., Nucl. Instr. Meth. A499 (2003) 659

- [ HARP ]: V. Ammosov et al., Nucl. Instr. Meth. A 588 (2008) 294 [ ALICE ]: (a) ALICE Collaboration, The ALICE Experiment, J. of Instr., JINST 3 S08002 (2008);
  - (b) R. Campagnolo, HEP 2005, Int. Europhysics Conf., EPS, Lisboa;
  - (c) B. Mota et al. NIM A 535 (2004) 500;
  - (d) J. Alme et al., arXiv:1001.1950v1.pdf (2010); nima.2010.04.042

## Figure Captions

- Fig. 1 Measurements of cluster size distributions. Full line: eye fit, dashed line: model prediction. [14]
- Fig. 2 Relativistic rise of ionization I, normalized to the minimum  $I_0$ , as function of p/mc=  $\beta\gamma$ . The curve is from simulation [18], the crosses are measurements [17].
- Fig. 3 Density dependence of the relativistic rise in Ar/CH<sub>4</sub> (90/10) [19].
- Fig. 4 Measured pulse height distribution for a 2.3cm sample in Ar/CH<sub>4</sub> at 1 atm: (a) 3GeV/c protons, (b) 2GeV/c electrons [19].
- Fig. 5 Electron collision cross-sections used in Magboltz [23, 11].
- Fig. 6 Characteristic electron energy  $\varepsilon_k$  derived from measurements of diffusion and drift velocity, as function of reduced electric field E/N for a 'hot' and a 'cold' gas, Ar and  $CO_2$ , respectively [25 (a), 7].  $10^{-17}Vcm^2=251V/cm$  atm at  $20^{\circ}C$ .
- Fig. 7 The fraction  $\Delta$  of energy lost per collision as function of mean energy  $\epsilon$  of the electron [24].
- Fig. 8 Computed drift velocities of electrons in a few gases [15, p. 293].
- Fig. 9 Drift velocities of singly charged ions of noble gases [28].
- Fig. 10 Transverse ( $D_T^*$ ) and longitudinal ( $D_L^*$ ) diffusion constants for electrons, the rms spread after 1cm drift. The dashed-pointed line indicates the thermal limit [31].
- Fig. 11 Transverse and longitudinal diffusion constants for electrons in Ar/CH<sub>4</sub> (80/20), in  $\mu$ m/cm<sup>1/2</sup>, as function of electric and magnetic fields. Drift velocity in  $\mu$ m/ns [33 b)].
- Fig. 12 Transverse diffusion measured in Ar/CH<sub>4</sub> mixtures at 600Torr after 15cm drift without magnetic field B and with B = 20.4 kG [4].
- Fig. 13 Measured 'First Townsend coefficient'  $\alpha$  in noble gases [7] and calculated  $\alpha$  in Ar/CH<sub>4</sub> mixtures(100-0 means 100%Ar) [41 (a)], with points from measurements [41 (b)].
- Fig. 14 Polya distributions [13].
- Fig. 15 Reconstructed tracks from laser beams in the ALEPH TPC [72].
- Fig. 16 Examples of deposits on  $20\mu$ m anode wires after strong irradiation [61].
- Fig. 17 Sketch of the PEP4 TPC [PEP4 (d)]
- Fig. 18 Schematic wire and pad layout in the PEP4 TPC proportional chambers [PEP4 (e)].
- Fig. 19 DELPHI TPC-Sector boundary: (a) Pulse height variation near the boundary with and without guard strip. (b) Details of the frames and guard strips at the boundary [48].
- Fig. 20 Schematics of the field lines for an open and closed gating grid [5].
- Fig. 21 Schematic cut through the field cage of the ALEPH TPC [5].
- Fig. 22 Performance of the ALTRO chip of the ALICE TPC: pulses from a high multiplicity cosmic ray event before and after tail cancellation and baseline restoration [70 (b)].
- Fig. 23 Definition of the track angles and the Lorentz angle  $\psi$  from **E** x **B** [72].

- Fig. 24 Spatial resolution measured with the ALEPH TPC:  $r\phi$  -resolution as function of pad crossing angle in  $r\phi$  and z-resolution as function of dip angle  $\lambda$  [72(b)]
- Fig. 25 Spatial resolution measured in the DELPHI TPC, as function of wire and pad crossing crossing angles,  $\alpha_w$  and  $\alpha_p$  [73 (b)].
- Fig. 26 Particle identification from ionization measurements (dE/dx) in the PEP4 TPC [15, p. 298].
- Fig. 27 Simulated and measured straggling functions (left) and truncated means (right) for protons [77].
- Fig. 28 Effect of fluctuations due to amplification and diffusion on the straggling function [77].
- Fig 29 Simulated straggling functions of protons for segments of different length x, normalized to x [78].
- Fig. 30 Separation power D from ionization sampling, obtained at 15GeV/c with 64 samples of 4cm [79].
- Fig. 31 A reconstructed event in the PEP4 TPC; rφ and rz views.
- Fig. 32 Mass separation by dE/dx in EOS [82].
- Fig. 33 Particle identification by dE/dx in the relativistic rise region from NA49 [83]
- Fig. 34 A reconstructed central Au-Au collision in STAR [84 (b)].
- Fig. 35 Particle identification in very high multiplicity events in STAR [84 (a)].
- Fig. 36 Pattern recognition in the liquid Argon TPC of ICARUS [91].
- Fig. 37 Principle of the Parallel Plate Avalanche Chamber [103].
- Fig. 38 Principle of the Pad TPC. The drift volume lies beyond the mesh [104].
- Fig. 39 A schematic cut through the Micromegas [113].
- Fig. 40 Principle of the GEM structure [113].

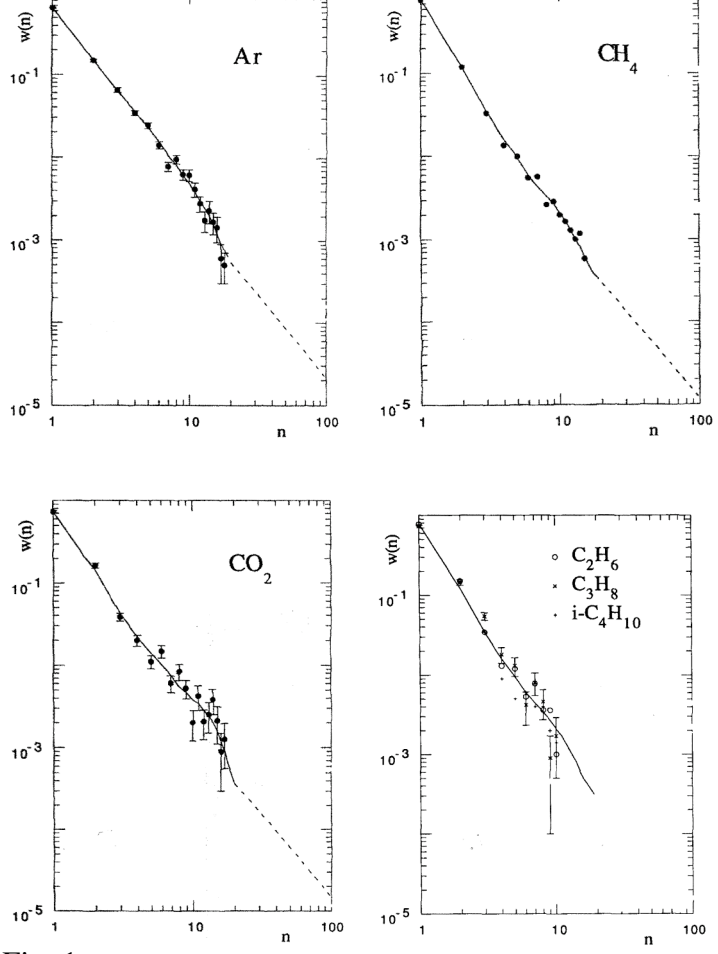


Fig. 1

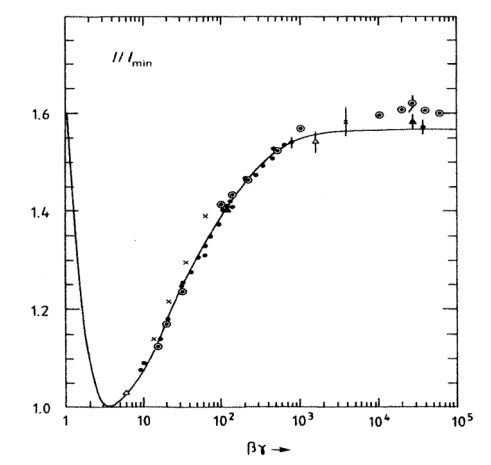


Fig. 2

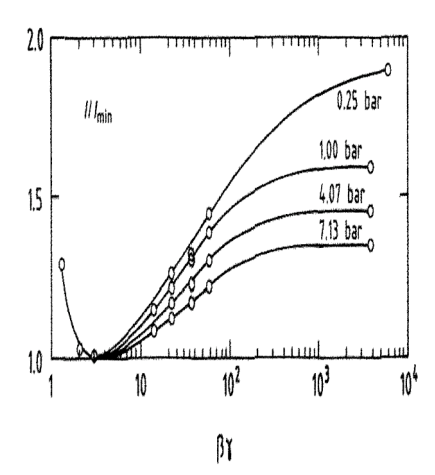


Fig. 3

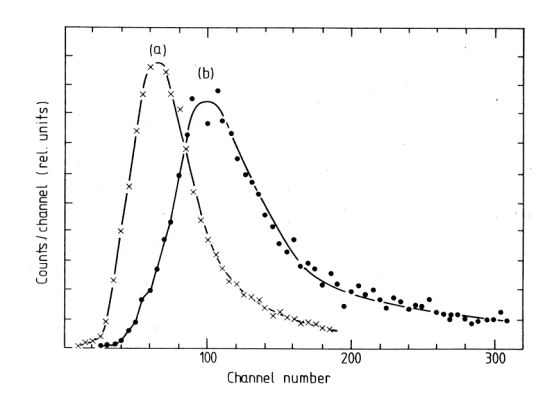
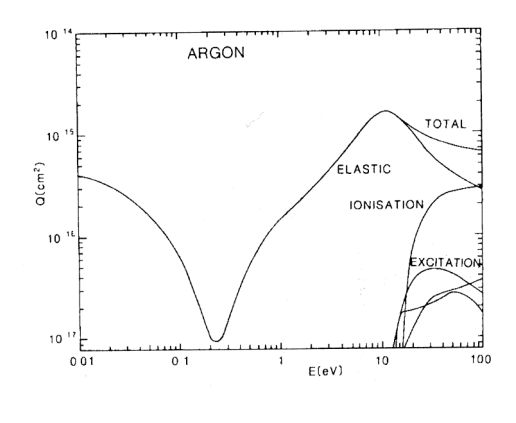
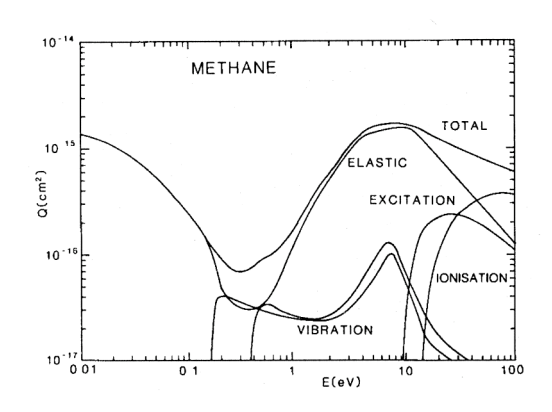
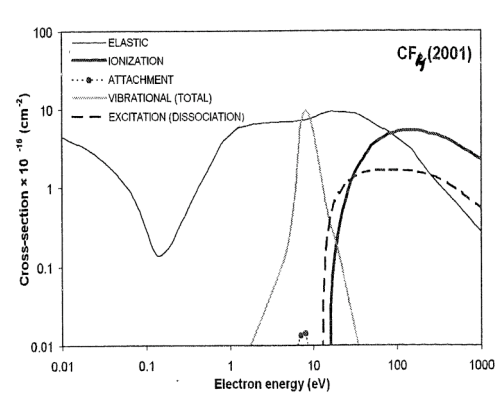


Fig. 4







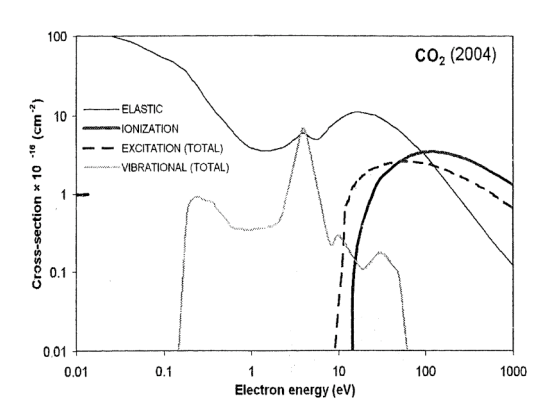


Fig. 5

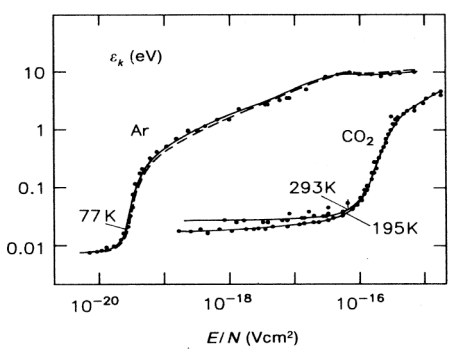


Fig. 6

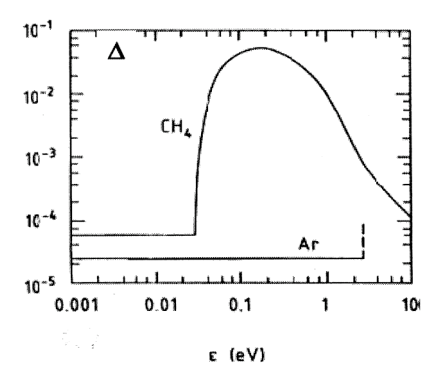


Fig. 7

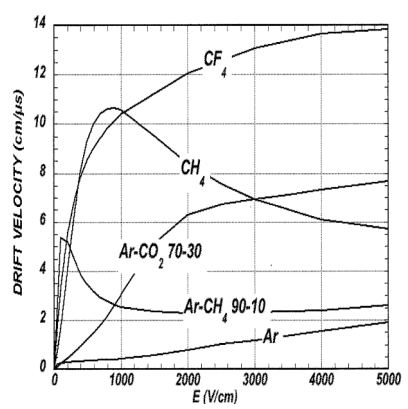


Fig. 8

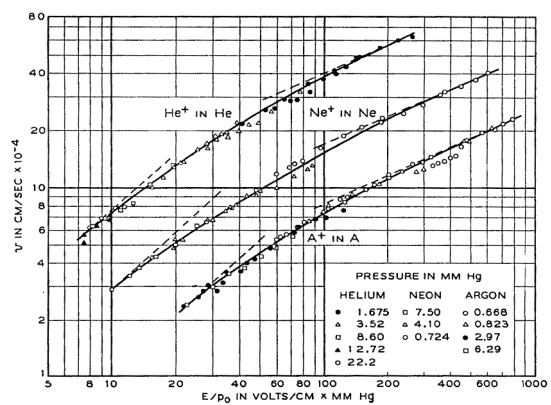


Fig.9

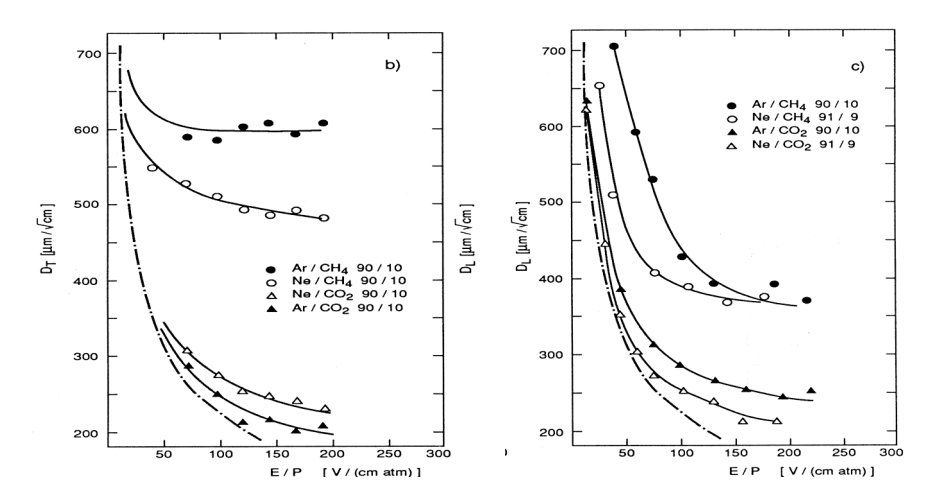


Fig. 10

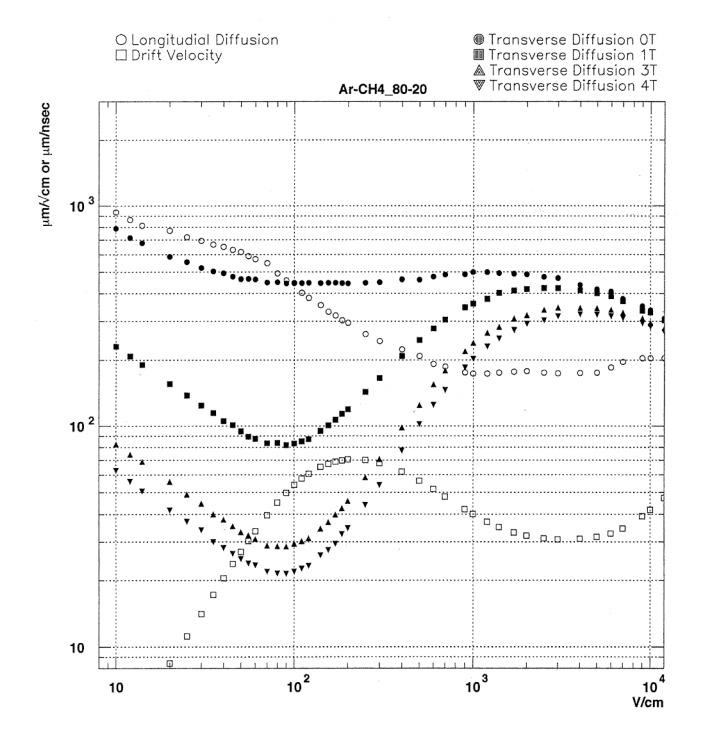
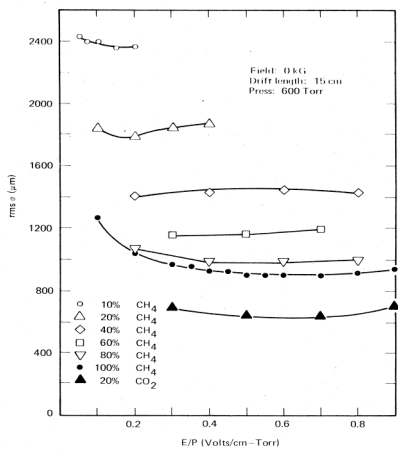


Fig. 11



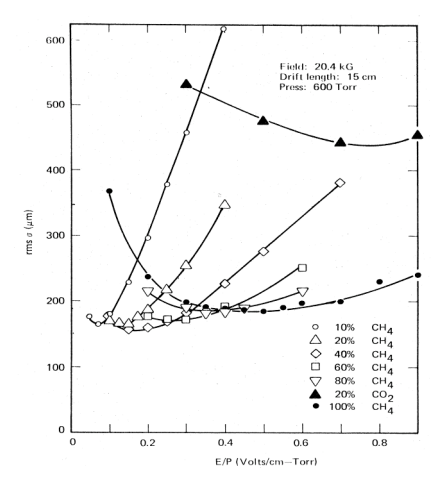


Fig. 12

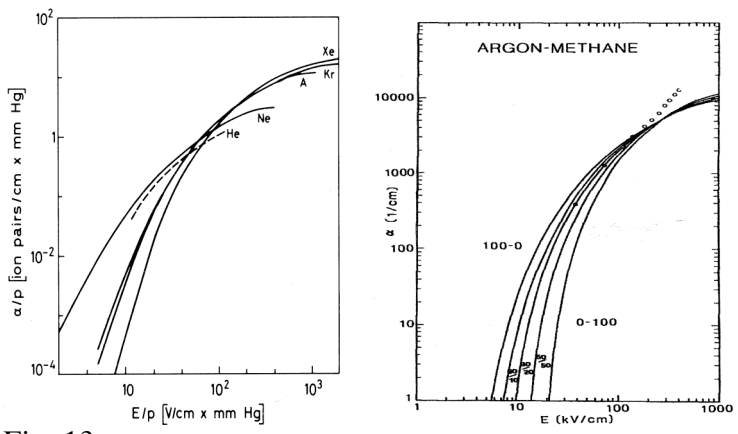


Fig. 13

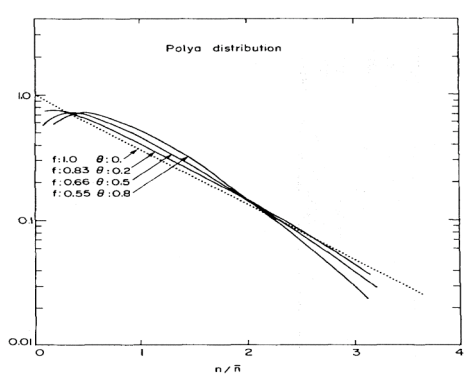


Fig. 14

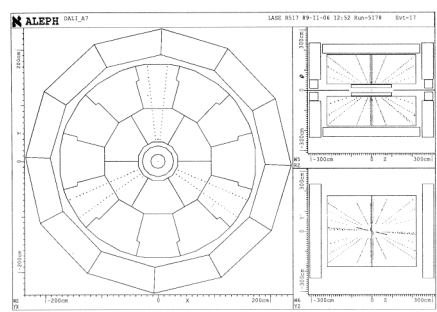


Fig. 15

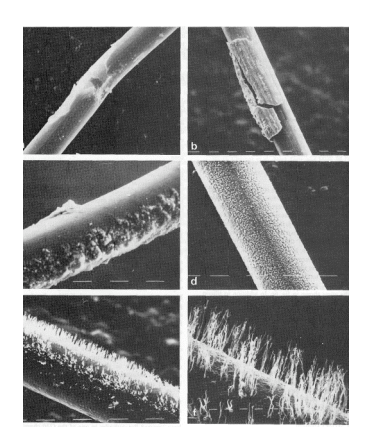


Fig. 16

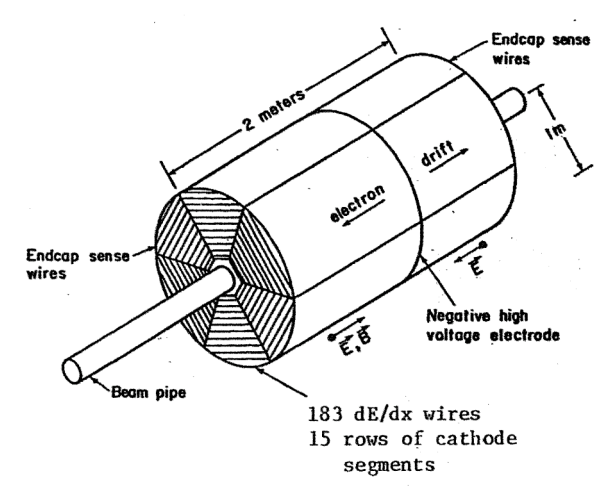


Fig. 17

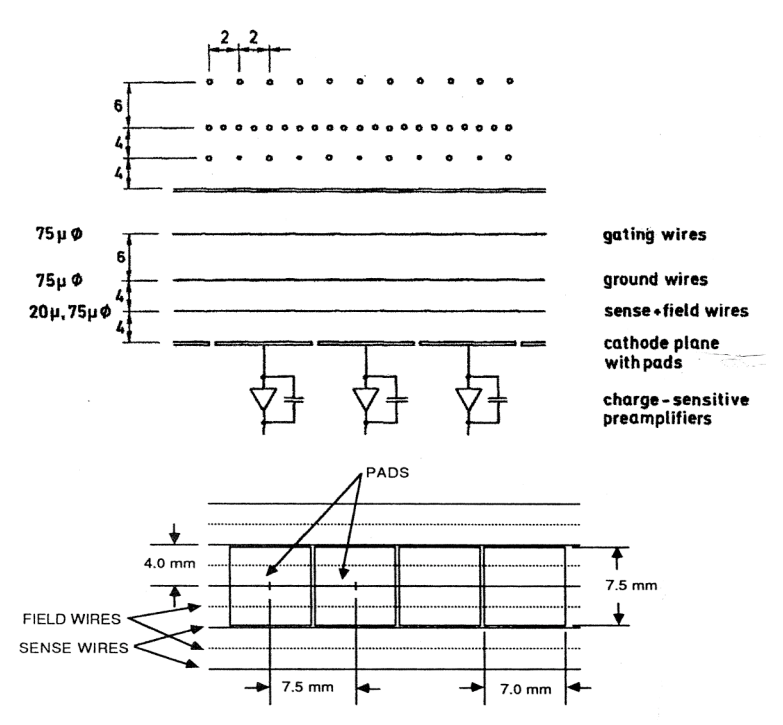
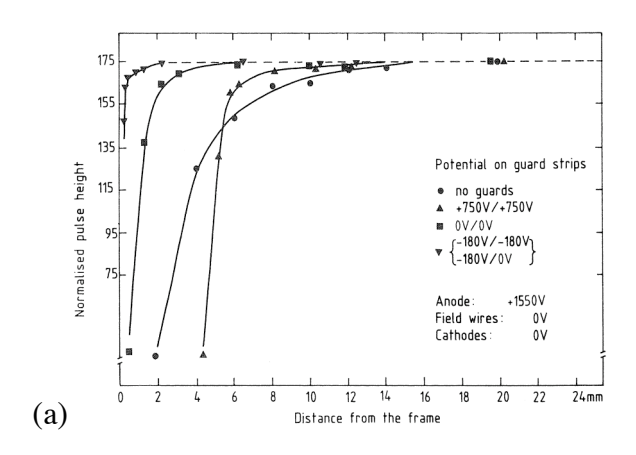


Fig. 18



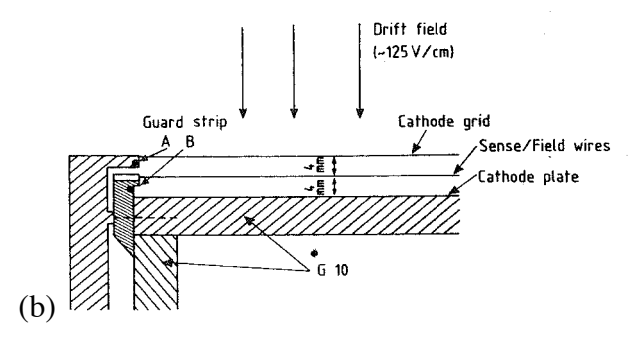


Fig. 19

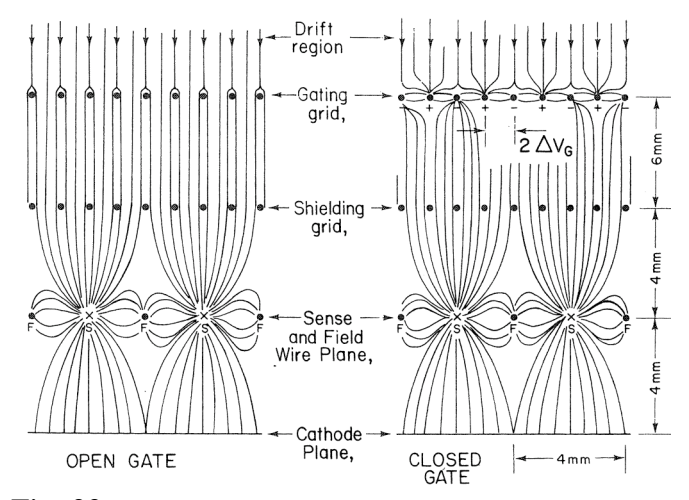


Fig. 20

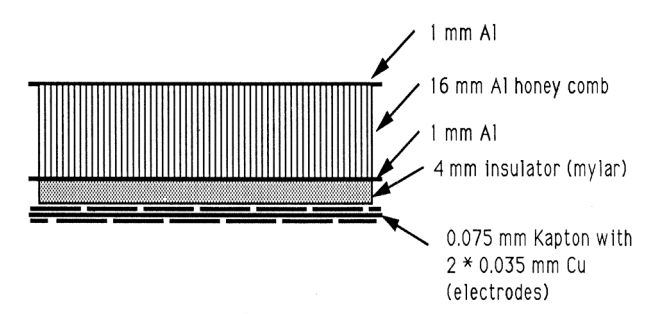


Fig. 21

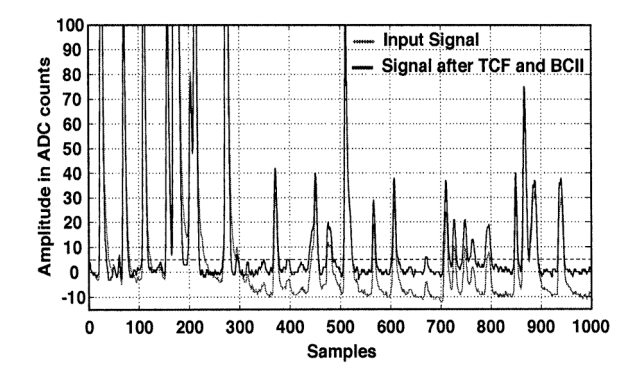


Fig. 22

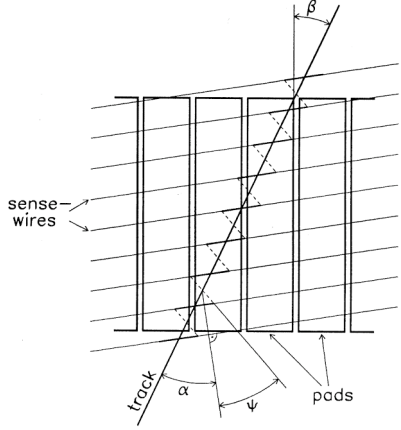


Fig. 23

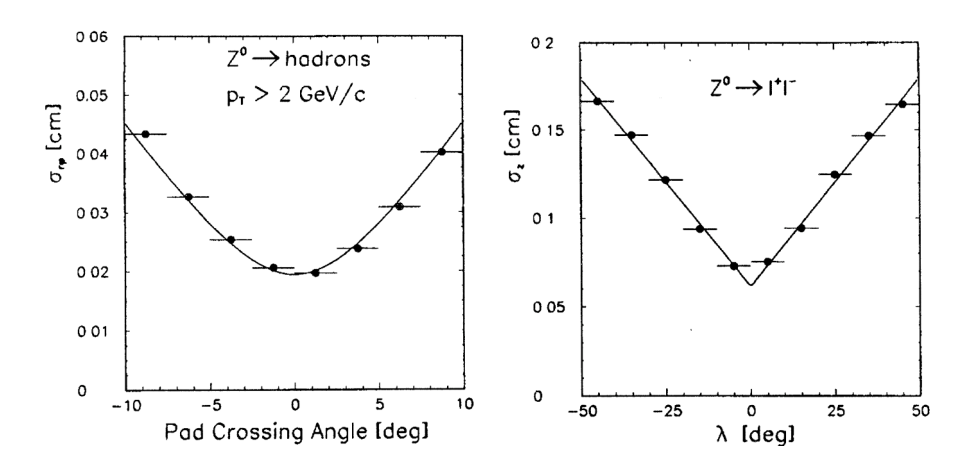


Fig. 24

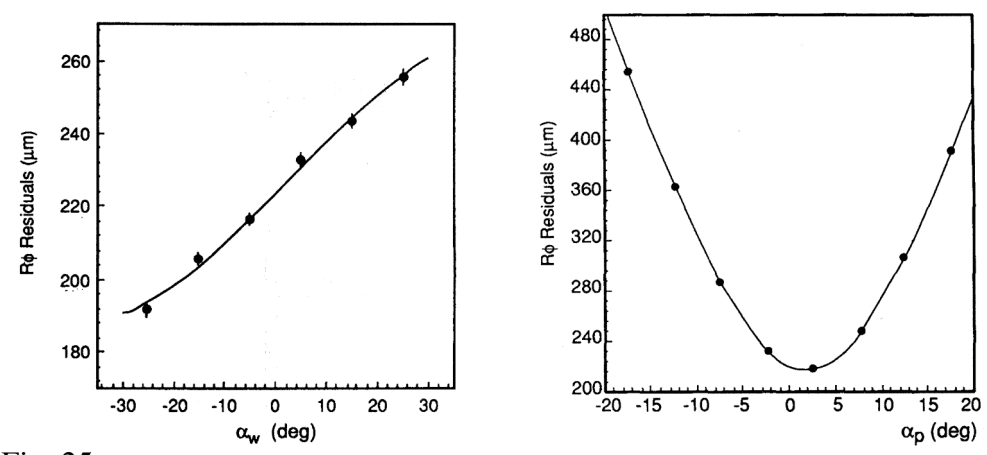


Fig. 25

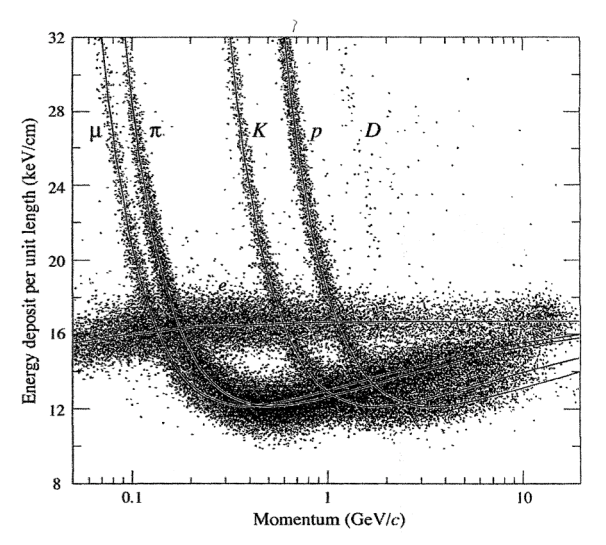


Fig. 26

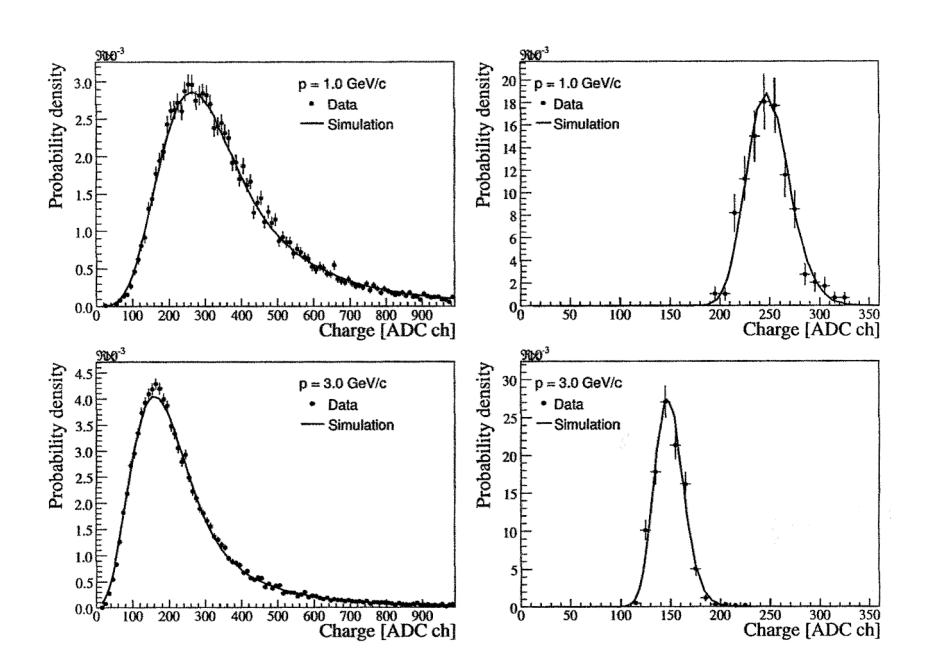


Fig. 27

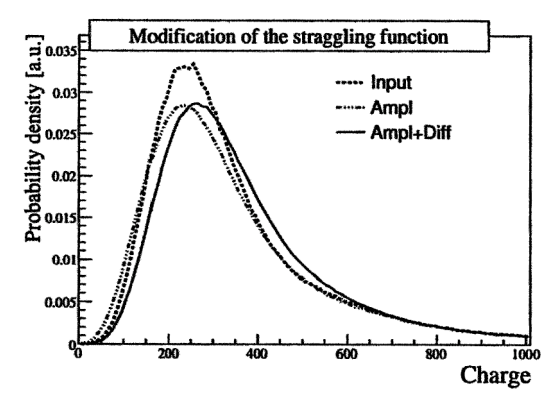


Fig. 28

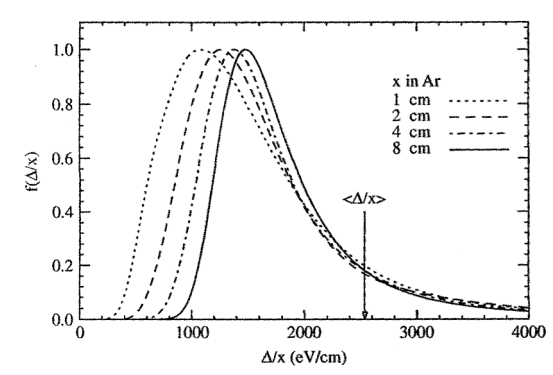


Fig. 29

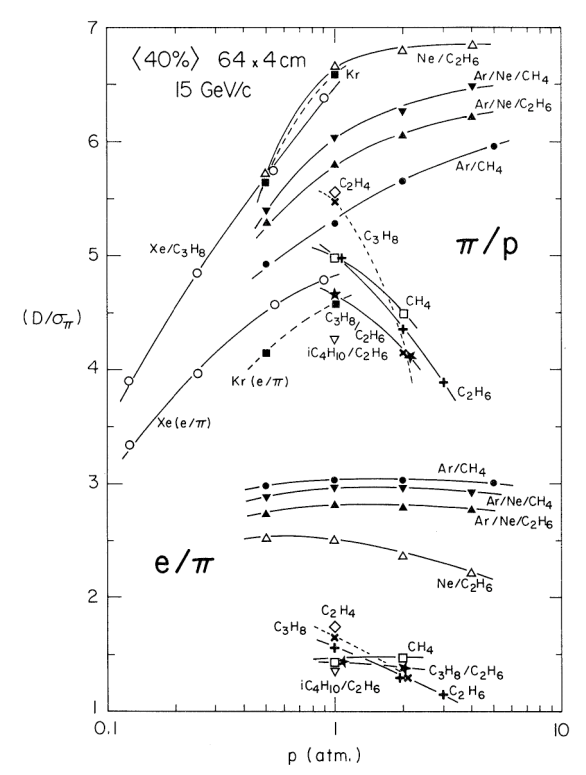


Fig. 30

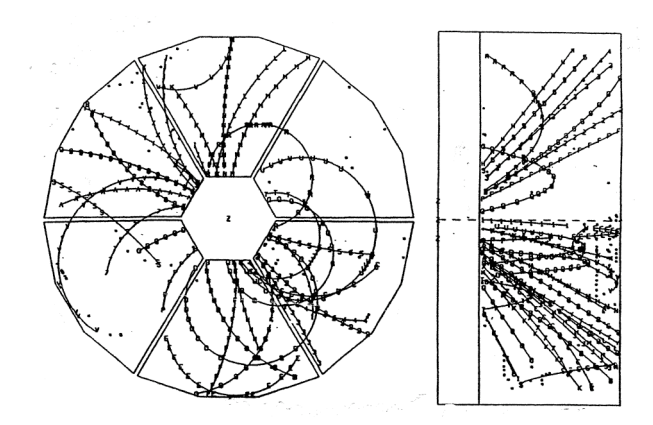


Fig. 31

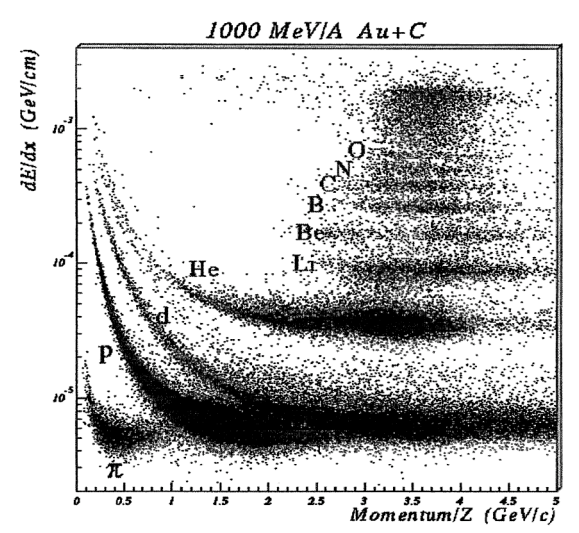


Fig. 32

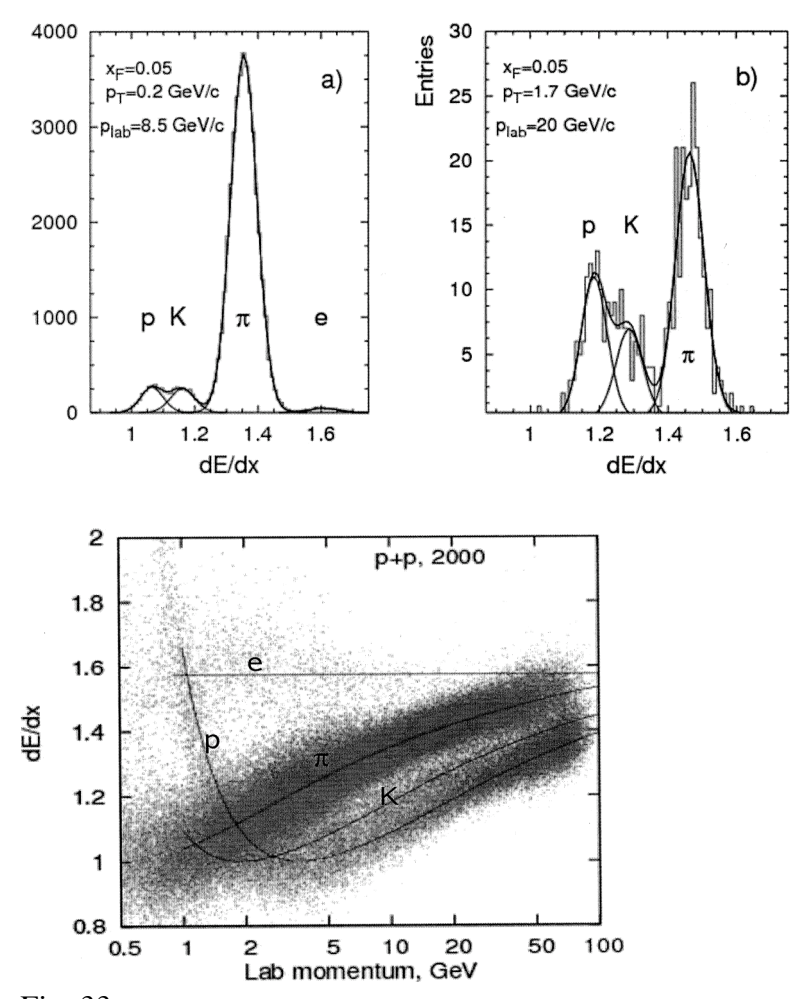


Fig. 33

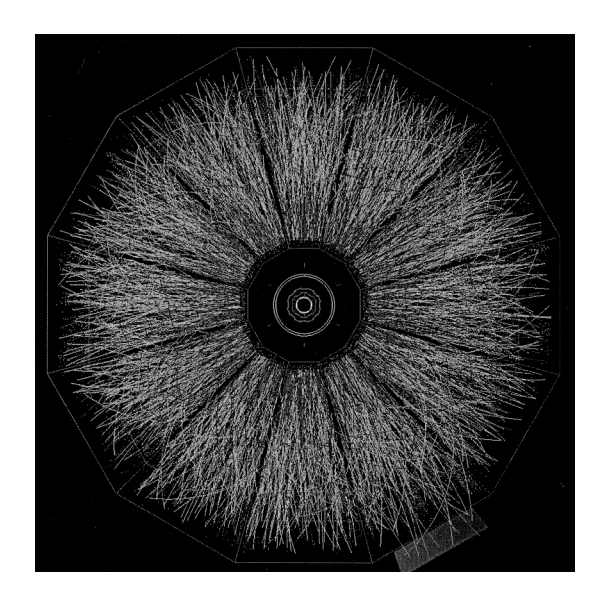


Fig. 34

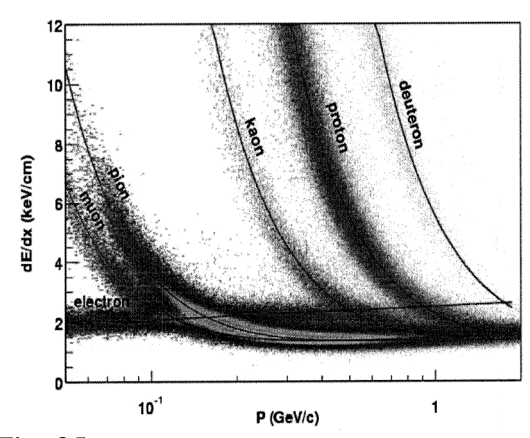


Fig. 35

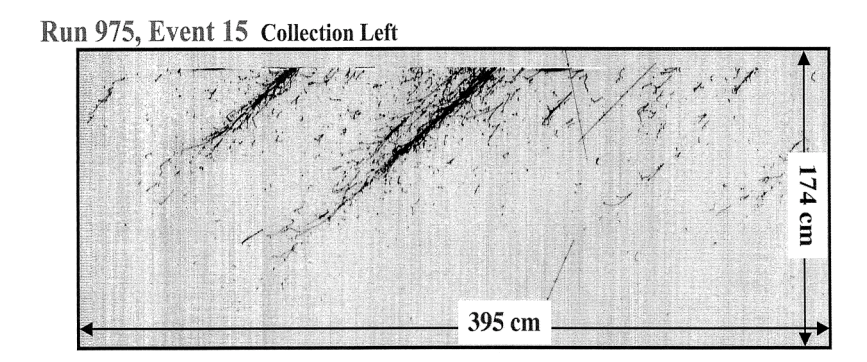


Fig. 36

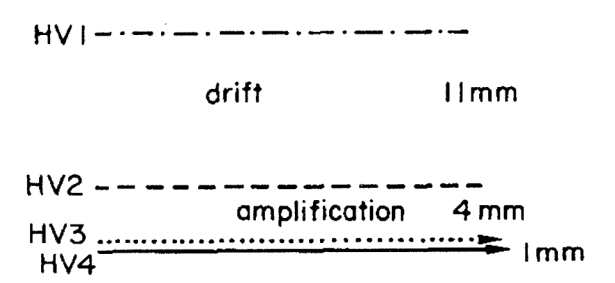


Fig. 37

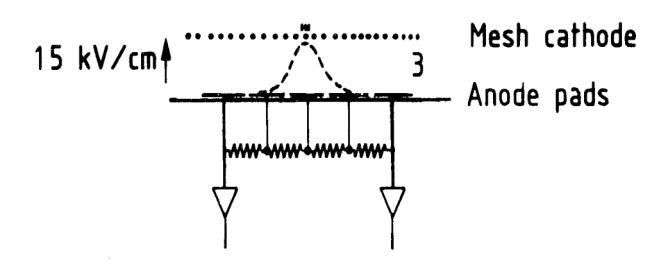


Fig. 38

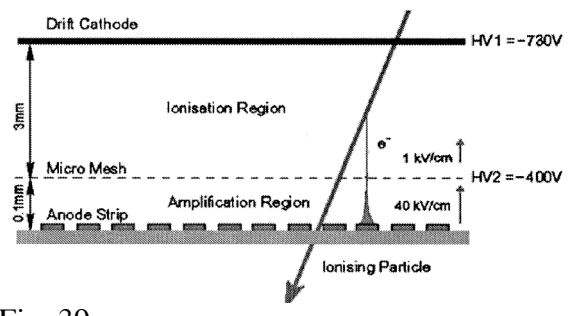
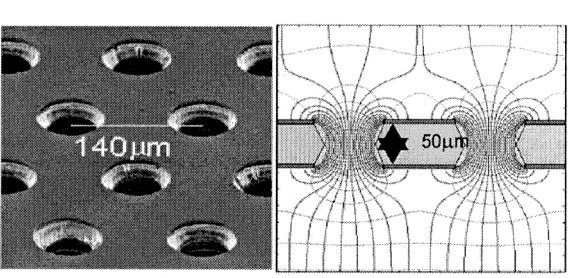
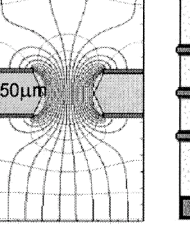


Fig. 39





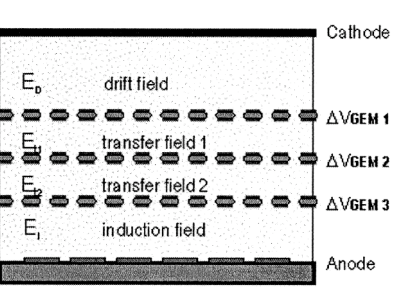


Fig. 40

PARAMETER / EXPERIMENT	PEP4	TRIUMF	TOPAZ	ALEPH	DELPHI	STAR	ALICE 1)
1. OPERATION	1982 / 1984	1982 / 1983	1987	1989	1989	2000	2009
INNER / OUTER RADIUS	0.2 / 1.0	~0.15 / 0.50	0.38 / 1.1	0.35 / 1.8	0.35 / 1.4	0.5 / 2.0	0.85 / 2.5
[m]	4	0.24	4.4	2.2	1.24	2.1	2.5
MAX. DRIFTLENGTH (L/2)	1	0.34	1.1	2.2	1.34	2.1	2.5
[m] MAGNETIC FIELD [T]	0.4 / 1.325	0.9	1	1.5	1.23	0.25 / 0.5	0.5
GAS:	Ar / CH4	Ar / CH4	Ar / CH4	Ar / CH4	Ar / CH4	Ar / CH4	Ne /CO2/ N2
Mixture	80 / 20	80 / 20	90 / 10	91/9	80 / 20	90 / 10	90/ 10/ 5
Pressure [atm]	8.5	1	3.5	1	1	1	1
DRIFT FIELD [KV / cm /	0.088	0.25	0.1	0.11	0.15	0.14	0.4
atm]	0.000	0.25		0.11	0115		
ELECTRON DRIFT	5	7	5.3	5	6.69	5.45	2.7
VELOCITY [cm/μsec]							
ωτ (see 2.2.1.3)	0.2 / 0.7	2	1.5	7	5	1.15 / 2.3	< 1
PADS: Size w•L [mm•mm]	7.5x7.5	(5.3-6.4)x19	(9-11)x12	6.2x30	~7x7	2.85x11.5	4x7.5
						6.2x19.5	6x10/15
Max. no. 3-D points	15 - straight	12	10 - linear	9+12 - circular	16 - circular	13+32 - straight	63+64+32
dE/dx: Max. no. samples/track	183	12	175	148+196	192	13+32	63+64+32
Sample size [mm atm]; w	4•8.5; wires	6.35; wires	4x3.5; wires	4 ; wires	4; wires	11.5 + 19.5;pads	7.5+10+15; pads
GAS AMPLIFICATION	1000	50 000		3000-5000	5000	3000/1100	20 000
GAP a-p; a-c; c-gate 2)	4; 4; 8	6	4; 4; 8	4; 4; 6	4; 4; 6	2; 2; 6 / 4; 4; 6	2; 2; 3 / 3; 3; 3
PITCH a-a; cathode; gate	4; 1; 1		4; 1; 1	4; 1; 2	4; 1; 1	4; 1; 1/4; 1; 1	2.5; 2.5; 1.5
PULSE SAMPLING [MHz/no. samples]	10/455, CCD	only 1 digitiz., ADC	10/ 455, CCD	11/512, FADC	14/ 300, FADC	9.6 / 400	5-10/500-1000, ADC
GATING 3)	≥1984 o.on tr.	≥1983 o.on tr.	o. on tr.	synchr. cl.wo.tr	static	o.on tr.	o.on tr.
PADS, total number	15 000	7800	8200	41 000	20 000	137 000	560 000
PERFORMANCE							
$\Delta x_T [\mu m]$ -best / typ.	130-200	200/	185/230	170/200-450	180/190-280	300-600	spec:800-1100
$\Delta x_1 [\mu m]$ -best / typ.	160-260	3000	335/900	500-1700	900	500-1200	spec:1100-1250
2-TRACK SEPARATION	20		25	15	15	8 - 13 / 30	
[mm], T / L							
$\partial p/p^2 [GeV/c]^{-1}$ : TPC alone; high p	0.0065		0.015	0.0012	0.005	0.006	spec:0.005
dE/dx [%] SINGLE TRACKS/ IN JETS	2.7 / 4.0		4.4 /	4.4 /	5.7 / 7.4	7.4 / 7.6	spec:4.9 / 6.8
COMMENTS		a in single PCs	chevron pads	circular pad	circular pad	No field wires	No field wires
		strong ExB effe	ct			> 3000 tracks	≤ 20 000 tracks

Expected performance
 a = anode, p = pads, c = cathode grid
 o. on tr.: gate opens on trigger; cl.wo.tr.: opens before collision and closes without trigger; static: closed for ions only (see text).

PARAMETER /	NA35	EOS / HISS	NA49 VTX	NA49 MAIN	CERES/NA45	HARP	T2K <sup>a</sup>
EXPERIMENT cont.							
1. OPERATION	1990	1992	1995	1995	1999	2001	2009/10
INNER / OUTER RADIUS or L	2.4 / 1.25 (L /	1.5 / 0.96 (L /	2.5 / 1.5 (L/W)	4 / 4 (L/W); 2x	0.6 / 1.3; L=2	0.1 / 0.41	2.2 / 0.7
/ W [m]	W)	W)	; 2x				(H/L); 3x
MAX. DRIFTLENGTH (L/2) [m]	1.12 vert.	0.75 (H)	0.67 vert.	1.1 vert.	0.7 rad.	1.6	0.9 W
MAGNETIC FIELD [T]	0	1.3	1.5	0	Bz < 0.7; Br < 0.3	0.7	0.2
GAS:	Ar / CH4	Ar / CH4	Ne / CO2	Ar / CH4 / CO2	Ne / CO2	Ar / CH4	Ar/CF4/i- C4H10
Mixture	91/9	90/10	90 / 10	90/5/5	80/20	91/9	95/3/2
Pressure [atm]	1	1	1	1	1	1	1
DRIFT FIELD [kV / cm / atm]	0.12	0.12	0.19	0.175	0.2-0.6	0.111	0.2
ELECTRON DRIFT VELOCITY [cm / µsec]	5	5.5	1.3	2.3	0.7-2.4	5.2	7
ωτ (see 2.2.1.3)	0	0.5	1	0		3.3	0.7
PADS: SIZE (w•L, mm•mm)	5.5x40	8x12	3.5x(16,28)	(3.6, 5.5)x40	10 chevron	6.5x15	6.9x9.7
Max. no. 3-D points	60+30	128	<150	90		20	72x3
dE/dx: MAX. NO.	60	128	<150	90		20	72x3
SAMPLES/TRACK							
Sample size [mm• atm]; w or	40; pads	12	16, 28	40		15	9.7
p							
GAS AMPLIFICATION		3000	20 000	5000	8000	20 000	~1000
Gap a-p; a-c; c-gate 2)		4; 4; 6	3,2;	2,3; 3; 6	3;3;6	5;5;6	0.128
PITCH a-a; cathode; gate	4; 1; 2	4; 1; 2	4; 1; 1	4; 1; 1	6; 2; 2	4; 2; 2 stagg.	
PULSE SAMPLING [MHz / no. samples]	12.5 /	10 / 256, SCA	/ 512	/ 512		10 / >300, FADC	/ 512 SCA
GATING 3)		o. on tr.	o. on tr.	o. on tr.	o. on tr.	o.on tr.	none
PADS, total number	11 000	15 000	74 000	108 000	78 000	4000	125 000
PERFORMANCE							
$\Delta x_T [\mu m]$ -best / typ.	300-800	300	150	150	230/340	600-2400	600 (1m drift)
$\Delta x_L [\mu m]$ -best / typ.	250-450	500	120	120	dr=400/ 640	3.5	ooo (Im anii)
2-TRACK SEPARATION [mm]	18	25		10	ui=100/ 010	3.3	
$\partial p/p^2$ [GeV/c] <sup>-1</sup> : TPC alone; high		1			1	0.2/0.45-0.50	spec: <10;
dE/dx [%]: single tracks / in jets	/ 6	/ 4	<4 : VTX + Ma	in		16	spec: <10 /
	-	-	, 222 . 1714				-F22. 120,
COMMENTS	B=0	only pad r.o.	Kr <sup>m</sup> calibration	up to 1200 tr.	Radial TPC	el. cross-talk	Micromegas r.o.
-	only pad r.o.		only pad r.o.	only pad r.o.	No field wires		
-	) F	1	7 F	) F		1	: